

RPM - the fast Random Particle-Mesh method to realize unsteady turbulent sound sources and velocity fields for CAA applications

R. Ewert*

DLR, Institute of Aerodynamics and Flow Technology

Technical Acoustics, Lilienthalplatz 7, 38108 Braunschweig, Germany

e-mail: roland.ewert@dlr.de

The simulation of broadband noise with CAA techniques is discussed. Unsteady broadband sound sources are modeled in the time-domain with a highly efficient computational method. The generated fluctuations reproduce very accurately autocorrelations and integral length-scales such as that provided by a RANS simulation of the time-averaged turbulent flow problem. It is argued that an approach based on synthetically generated sources has to be seen as an algorithmic extension of traditional statistical broadband methods in the frequency domain. Fluctuating quantities are generated by spatially filtering convective white-noise. The discrete realization of convective white-noise is based on random particles that are advanced using an area-weighted mean of the mean-flow from neighboring mesh points. The spatial filtering is realized by interpolating the random values with a particle shape function onto the neighboring mesh points and applying subsequently a sequence of 1D filtering operations. Sample results for different aeroacoustic applications of the method are presented.

I. Introduction

THE prediction of turbulence related broadband noise, which arises e.g. in turbulent jets and due to turbulence-airframe interactions, is an important task in aeroacoustics. Today, broadband prediction methodologies of different levels of maturity are available, such as semi-empirical prediction schemes, analytical methods, and numerical high-fidelity methods like Large Eddy Simulation (LES) to resolve the fully unsteady problem. High-fidelity simulation tools have been applied successfully to various noise source problems. But they are computationally expensive and as such they are mainly applied in the research environment today.

In the industrial environment, and in particular for design purposes, for the foreseeable future broadband noise predictions of high Reynolds number flow problems will probably rely on simplified approaches. Analytical broadband methods in the frequency domain usually utilize a statistical description of the turbulence source features. Turbulent source statistics can be modeled through relatively simple mathematical expressions. One often used two-point correlation function to describe turbulent fluctuating quantities is based on a Gaussian function for the spatial and exponential or Gaussian functions for the temporal correlation. The well documented application of such approaches to generic airframe noise as well as jet noise problems often have shown very good agreement with measured broadband spectra. However, the application to an explicit problem in a purely analytical approach demands to introduce considerable simplifications in the considered geometries and flow properties (e.g. semi-infinite flat plates, constant flow). Therefore, it is consequent to involve numerical techniques for a further extension of statistical methods to more realistic geometries and problems in the design environment. For example, the turbulence length-scale and kinetic energy distribution of a Reynolds Average Navier-Stokes (RANS) solution has been utilized in the past for a more detailed statistical source description that covers a much wider range of geometries and flow conditions.

*Research Engineer, DLR, Institute of Aerodynamics and Flow Technology, Technical Acoustics, Braunschweig, Germany, AIAA Member.

In this framework the Random Particle-Mesh (RPM) method was introduced recently as a fast and efficient approach to set up fluctuating acoustic sound sources in the time-domain, whose statistics realize the characteristic Gaussian two-point correlations of statistical methods. The RPM method provides very accurately target turbulence length-scales and kinetic energy distributions such as that provided by RANS. The fluctuating acoustic sources can be used for a direct (primal) CAA approach. The applications of CAA techniques allows to consider complex mean-flow fields and geometries without any simplifications. A direct broadband approach in the time-domain yields equivalent results to a frequency domain method if the two-point space-time source statistics coincide, but unlike the latter needs only one computation to achieve spectra in a large number of observer points.

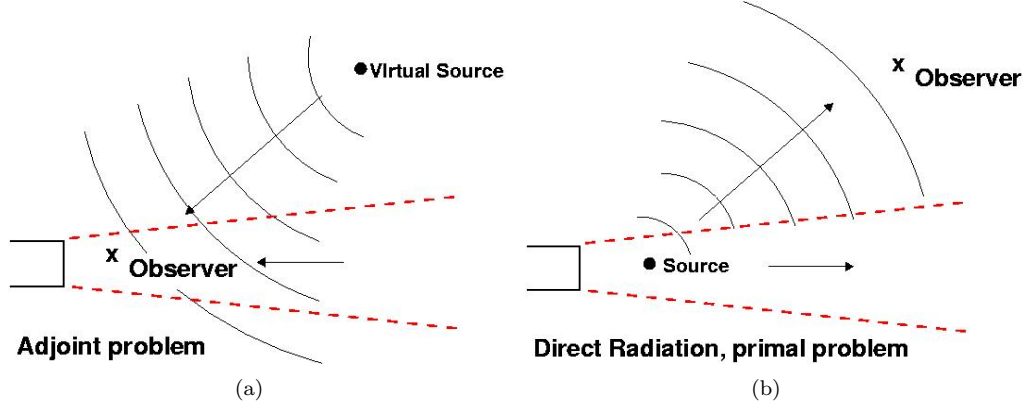


Figure 1. Adjoint and primal jet-noise problem.

For example, Fig. 1 shows a schematic of the approach proposed by Tam & Auriault¹ to determine the flow Green's functions that include jet refraction effects. Tam & Auriault utilize the adjoint linearized Euler equations (LEE) to compute the flow Green's functions in the jet source region with CAA techniques. From acoustic reciprocity the Green's value for the complete jet can be computed for the original observer position (becoming the virtual source position in the adjoint problem) for one single frequency. This gives $n \times m$ computations for n observer positions and m frequency bands. A broadband CAA approach to solve the primal LEE in the time-domain, on the contrary, allows to obtain the solution for all m frequency bands and n observers with one single computation. For this, however, an unsteady source has to be modeled, which realizes the appropriate two-point space-time correlations.

This work reports about the progress made with the RPM method, e.g., it has been extended to cover recirculation areas in the mean-flow domain and a simplified filter kernel was introduced that yields further increased efficiency while approximating the Gaussian correlation function through a cubic spline with limited support. Furthermore the method is applied for a time-domain realization of the Tam & Auriault approach to predict fine scale turbulence related noise. Sample results for jet noise, flat plate trailing edge noise as well as high-lift slat noise are presented.

II. Stochastic sound source modeling

A. Stochastic fluctuating fields via RPM

A widely used function to model the two-point space-time correlation $\mathcal{R}(\mathbf{x}, \mathbf{r}, \tau) = \overline{\psi(\mathbf{x}, t)\psi(\mathbf{x} + \mathbf{r}, t + \tau)}$ of a turbulent quantity $\psi(\mathbf{x}, t)$ in statistical noise approaches is based on Gaussian and exponential functions for the spatial and temporal correlations. This correlation function can be written as

$$\mathcal{R}(\mathbf{x}, \mathbf{r}, \tau) = \hat{R} \exp \left[-\frac{|\tau|}{\tau_s} - \frac{\pi(\mathbf{r} - \mathbf{u}_c \tau)^2}{4l_s^2} \right]. \quad (1)$$

The parameters τ_s and l_s define respectively the correlation time- and length scales and \hat{R} denotes the mean-square (MS) value of the correlated quantity for vanishing separation space \mathbf{r} and time τ . Taylor's hypothesis is taken into account by the convection velocity \mathbf{u}_c . For inhomogeneous turbulence τ_s , \mathbf{u}_c , l_s , and \hat{R} depend on position \mathbf{x} .

The Random Particle Mesh (RPM) method, which was introduced in Refs.,²⁻⁴ is capable of generating spatially and temporally fluctuating quantities whose statistics reproduce very accurately and efficient target two-point space-time correlations of the type described by eq. (1), whereby local target values for the parameters are realized. The fluctuating quantity $\psi(\mathbf{x}, t)$ is generated by spatially filtering a white-noise field. The procedure can be expressed through a continuous convolution or spatial filtering integral, which reads for an n -dimensional problem

$$\psi(\mathbf{x}, t) = \underbrace{\int \cdots \int_{A_S}}_{n \times} \hat{A}(\mathbf{x}') G^0(|\mathbf{x} - \mathbf{x}'|, l_s(\mathbf{x}')) \mathcal{U}(\mathbf{x}') d\mathbf{x}'. \quad (2)$$

The integration area A_S corresponds to the source patch in which unsteady sources are realized. In eq. (2) G^0 is a filter kernel, \hat{A} is a local amplitude functions, \mathcal{U} denotes the spatiotemporal white-noise field with properties defined below, and ψ is the realized fluctuating quantity. The filter kernel is normalized such that $\overline{\psi(\mathbf{x}, t)\psi(\mathbf{x}, t)} = 1$ for $\hat{A} = 1$. The argument of the filter kernel indicate that it is a function of the separation distance $|\mathbf{x} - \mathbf{x}'|$, and of the position-dependent kernel width l_s . The amplitude function in general depends on position as well.

The white-noise in eq. (2) is defined to have special spatio-temporal properties. For the simulation of frozen turbulence, e.g., the spatiotemporal white-noise field is uniquely defined by the properties

$$\overline{\mathcal{U}(\mathbf{x}, t)} = 0, \quad (3)$$

$$\overline{\mathcal{U}(\mathbf{x}, t)\mathcal{U}(\mathbf{x} + \mathbf{r}, t)} = \delta(\mathbf{r}), \quad (4)$$

$$\frac{D_0}{Dt}\mathcal{U} = 0, \quad (5)$$

where $\delta(\mathbf{r})$ denotes a multi-dimensional Dirac δ -function, which e.g. reads in 2D $\delta(\mathbf{r}) = \delta(r_1)\delta(r_2)$. Eq. (5) introduces the convection property into the fluctuation model through the passive convection of the white-noise field in a mean-flow \mathbf{u}_0 . It is to be understood such that in a locally comoving frame of reference the spatiotemporal white-noise field remains locally static. This condition can be satisfied even for an ideal white-noise realization (which is non-differentiable) although the substantial time derivative $D_0/Dt = \partial/\partial t + \mathbf{u}_0 \nabla$ involves spatial and temporal derivatives. As will be discussed subsequently in more detail, the spatial filtering in eq. (2) causes the δ -correlated white-noise field to be smeared out over a surrounding area, such that the generated fluctuating quantity ψ shows a larger correlation length-scale. It is evident that the correlation length-scale must be a function of the filter kernel width. However, for a vanishing filter kernel width, i.e. if it changes into a δ -function, the filtered quantity ψ will preserve the properties of the white-noise field. In other words, for very small correlation length scales the modeled fluctuating quantity ψ will convect at the local mean-flow velocity. For larger turbulent structures the convection velocity will be an average over the surrounding mean-flow flow field. This feature is intended to model the convection of turbulent structures in a flow-field, which might agree for very small vortices with the local mean-flow, however can deviate from it if the turbulent vortices have a size comparable to mean-flow length scales. For example, it is well known that the convection velocity in turbulent boundary layers (BL) approaches approximately $u_c \approx 0.6 \dots 0.7u_\infty$, where u_∞ denotes the flow velocity outside the BL. Therefore, the convection velocity, which appears in the correlation function eq. (1) as a parameter that has to be appropriately modeled, is implicitly fixed in the RPM framework through the local turbulent length scale $l_s(\mathbf{x})$ used in eq. (2) and the mean-flow field $\mathbf{u}_0(\mathbf{x})$ used in eq. (4). The convection acoustic sources is deemed to be an essential feature in the modeling of jet-noise or airframe noise sources. For example, without convection the proper Mach number scaling laws cannot be achieved.

The definition eq. (4) has to be satisfied for each point in the source domain where \mathcal{U} is defined, whereas the convection equation (5) determines the solution to be completely prescribed by the values on the inflow boundary of the source domain. It is shown in the Appendix that the constraints eq. (4) and eq. (5) can be satisfied simultaneously.

In Refs.²⁻⁴ it was shown that the spatial normalized correlation function $\mathcal{R}^0(\mathbf{r}, \tau)$, which is defined by

$$\mathcal{R}^0(\mathbf{r}, \tau) := \frac{\overline{\psi(\mathbf{x} + \mathbf{r}, t + \tau)\psi(\mathbf{x}, t)}}{\overline{\psi(\mathbf{x}, t)\psi(\mathbf{x}, t)}}, \quad (6)$$

and satisfies $\mathcal{R}^0(\mathbf{0}, 0) = 1$, is related for a n -dimensional problem to the filter-kernel function G^0 via

$$\mathcal{R}^0(\mathbf{r}, 0) = \underbrace{\int \cdots \int}_{n \times} G^0(\mathbf{r} - \boldsymbol{\xi}) G^0(\boldsymbol{\xi}) d\boldsymbol{\xi}. \quad (7)$$

This relation is a consequence of eq. (4). Using eq. (7), it can be shown that a Gaussian correlation function

$$\mathcal{R}^0(\mathbf{r}, 0) = \exp\left(-\frac{\pi}{4} \frac{|\mathbf{r}|^2}{l_s^2}\right). \quad (8)$$

is generated through the Gaussian filter kernel

$$G^0(\mathbf{r}) = \exp\left(-\frac{\pi}{2} \frac{|\mathbf{r}|^2}{l_s^2}\right), \quad (9)$$

whose width is a factor $2^{-1/2}$ smaller in comparison with that of the correlation function. Although filter kernels of other correlation functions could be derived from eq. (6) as well, a n -dimensional Gaussian filter kernel is advantageous in such that he has the property to be separable into a sequence of n one-dimensional filtering operations, which allows for a very efficient numerical discretization.

For a constant mean-flow \mathbf{u}_0 , the convection equation (5) is solved by $\mathcal{U}(\mathbf{x}, t) = \mathcal{U}_0(\mathbf{x} - \mathbf{u}_0 t)$, where $\mathcal{U}_0(\mathbf{x})$ shall indicate the white-noise field at time-level $t = 0$. Consequently, the relationship $\mathcal{U}(\mathbf{x} + \mathbf{r}, t + \tau) = \mathcal{U}_0(\mathbf{x} + \mathbf{r} - \mathbf{u}_0 \tau - \mathbf{u}_0 t) = \mathcal{U}(\mathbf{x} + \mathbf{r} - \mathbf{u}_0 \tau, t)$ holds. Using this relation, the white-noise property (4) becomes for $\tau \neq 0$

$$\overline{\mathcal{U}(\mathbf{x}, t) \mathcal{U}(\mathbf{x} + \mathbf{r}, t + \tau)} = \overline{\mathcal{U}(\mathbf{x}, t) \mathcal{U}(\mathbf{x} + \mathbf{r} - \mathbf{u}_0 \tau, t)} = \delta(\mathbf{r} - \mathbf{u}_0 \tau).$$

Using the last expression the extension of eq. (7) to non-vanishing time separations $\tau \neq 0$ can be deduced. For the constant mean-flow case it follows by simply substituting $\mathbf{r} - \mathbf{u}_0 \tau$ for \mathbf{r} on the right-hand side of eq. (7), which becomes

$$\mathcal{R}^0(\mathbf{r}, \tau) = \underbrace{\int \cdots \int}_{n \times} G^0(\mathbf{r} - \mathbf{u}_0 \tau - \boldsymbol{\xi}) G^0(\boldsymbol{\xi}) d\boldsymbol{\xi}. \quad (10)$$

Accordingly, the Gaussian filter kernel eq. (9) yields as an extension of eq. (8) a normalized spatial correlation with non-vanishing time separation τ of the form

$$\mathcal{R}^0(\mathbf{r}, \tau) = \exp\left\{-\frac{\pi |\mathbf{r} - \mathbf{u}_0 \tau|^2}{4l_s^2}\right\}. \quad (11)$$

Note that eq. (1) takes on the form realized through eq. (11) for $\mathbf{u}_c = \mathbf{u}_0$ and $\tau_s \rightarrow \infty$, i.e., for frozen turbulence. That is, in the constant mean-flow case the RPM convection velocity corresponds to \mathbf{u}_0 , irrespective of the actual correlation length l_s . To introduce an additional exponential temporal correlation as in (1) the homogeneous convection equation (5) has to be modified into a Langevin equation. The numerical discretization of an exponential temporal correlation will be discussed in section E.

Rigorously, the results presented so far are restricted to homogeneous filter kernels that realize constant correlations and length-scales throughout the source domain. Local kernels that realize inhomogeneous correlations and length-scales can be also deduced. However, the variation of these stationary quantities is usually small compared to the turbulent length-scale itself. Numerical test indicated the analytical findings for homogeneous filter kernels to be also valid with good accuracy for length scales $l_s(\mathbf{x}')$ and kernel amplitudes $\hat{A}(\mathbf{x}')$ not locally varying too strong. The amplitude has to be chosen such that the local mean-square values \hat{R} in eq. (1) equals a target value. Appropriate values for \hat{R} can be found utilizing the results from statistical broadband noise approaches.

B. Numerical discretization of the RPM method

In the discretization of the RPM method the continuous integral eq. (2) is approximated through the finite sum

$$\psi(\mathbf{x}, t) = \sum_{i=1}^M G_i(\mathbf{x}) r_i(t). \quad (12)$$

Eq. (12) follows by splitting the source domain A_S in eq. (2) into M non-overlapping control volumes ΔA_i and by approximating the integral through the summation over all control volumes. Here the index i indicates the i th control volume ΔA_i of the source domain. The amplitude \hat{A} is absorbed in the filter kernel, i.e. $G_i(\mathbf{x}) = G(\mathbf{x}, \mathbf{x}'_i) = \hat{A}(\mathbf{x}'_i)G^0(\mathbf{x}, \mathbf{x}'_i)$. The spatial coordinate \mathbf{x}'_i denotes a point on the i th control volume. It is advantageous to evaluate the filter kernel at the cell center

$$\mathbf{x}_i^s = \frac{1}{\Delta A_i} \int_{\Delta A_i} \mathbf{x}' d\mathbf{x}' \quad (13)$$

of control volume ΔA_i , i.e. $G_i(\mathbf{x}) := \hat{A}_i(\mathbf{x}_i^s)G_i^0(\mathbf{x}, \mathbf{x}_i^s)$. Note that for simplicity in the following multi-dimensional integration is indicated through one single integral. The quantity r_i in eq. (12) is a random value defined through

$$r_i(t) = \int_{\Delta A_i} \mathcal{U}(\mathbf{x}', t) d\mathbf{x}'. \quad (14)$$

Let $\langle \mathcal{U}_i \rangle := r_i / \Delta A_i$ be the average of the white noise field over ΔA_i , then eq. (12) is

$$\psi(\mathbf{x}, t) = \sum_{i=1}^M G_i(\mathbf{x}) \langle \mathcal{U}_i \rangle \Delta A_i. \quad (15)$$

Since $\langle \mathcal{U}_i \rangle \rightarrow \mathcal{U}_i$ holds in the limit of infinitely small subdomains $\Delta A_i \rightarrow 0$, the eq. (15) - and thus eq. (12) - is a consistent approximation to eq. (2). Two basic approximations are introduced in eq. (15):

1. $\langle \mathcal{U}_i \rangle$ is a filtered approximation to \mathcal{U}_i ,
2. the summation is a fourth order accurate approximation to the integral based on $\langle \mathcal{U}_i \rangle$ as the underlying white-noise field,

please refer to Section A of the Appendix for further details.

The local integration of the white-noise field over ΔA_i in eq. (14) can be deemed a low-pass filter applied to the field \mathcal{U} at point i , which causes a spectral cut-off of the spectrum corresponding to $\langle \mathcal{U}_i \rangle$. As long as this cut-off wave number is larger than the highest wave-number to be resolved by the fluctuating streamfunction, such an approximation has only little effect on the resolved scales. All further properties of r_i can be derived from the definitions eqs. (3-5) of the spatiotemporal white-noise field \mathcal{U} . Due to eq. (3) and definition eq. (14) the random value exhibits the property $\overline{r_i} = 0$. Using definition eq. (4), the correlation of the random values becomes

$$\overline{r_i r_j} = \int_{\Delta A_i} \int_{\Delta A_j} \delta(\mathbf{x} - \mathbf{x}') d\mathbf{x} d\mathbf{x}' = \begin{cases} 0 & \text{if } i \neq j \\ \Delta A_i & \text{if } i = j \end{cases} \quad (16)$$

That is, r_i is a fluctuating quantity with zero mean and mean-square value $\overline{r_i^2} = \Delta A_i$. Since we consider statistically stationary broadband problems, time averaging and ensemble averaging can be exchanged, the latter indicated by $\langle \cdot \rangle$. Taking into account that a sequence of random values in the range $\pm\sqrt{3}$ realizes a root-mean-square (RMS) of 1, the value r_i at source location i for one single realization of an ensemble can be found by choosing for it a random value in the range $\pm\sqrt{3\Delta A_i}$. This guarantees $\langle r_i^2 \rangle = \overline{r_i^2} = \Delta A_i$ to be satisfied.

According to eq. (5) the white-noise field remains locally static in a comoving frame of reference. That is, if $\Delta A'_i$ describes a convecting control volume, whose boundary curve is drifting in the mean-flow and corresponds for $t = t_0$ with that of a fixed control volume ΔA_i , the random value r_i defined by the integral eq. (14) applied to control volume $\Delta A'_i$ is independent of time in incompressible mean-flow^a. In a second order consistent approximation the cell center of $\Delta A'_i$ convects with its local mean-flow velocity

$$\dot{\mathbf{x}}_i^s = \mathbf{u}_0(\mathbf{x}_i^s) + \mathcal{O}(h^2), \quad (17)$$

see Section B for further clarifications on the last statements.

The discretization can be interpreted such that the source domain A_S is resolved by M discrete particles at moving locations \mathbf{x}_i^s . Each particle carries (in low Mach number flow) a frozen random value r_i in the

^aFor compressible 2D mean-flow the control volume changes its magnitude ($\rho_0 \Delta A_i$ is conserved) such that $\rho_0 r_i$ remains constant.

range $\pm\sqrt{3\Delta A_i}$ and drifts with the local mean-flow velocity through the source domain, Fig. 2(a). In this picture the random values r_i represents the white-noise field for the surrounding control volume ΔA_i . To evaluate the fluctuating quantity ψ for discrete points \mathbf{x}_j (e.g. on a CAA mesh), it is computed with eq. (12) by summing over all particles, i.e.

$$\psi_j = \psi(\mathbf{x}_j) = \sum_{i=1}^N G_{ji} r_i.$$

Here G_{ij} indicates evaluations of the filter kernel function for discrete points \mathbf{x}_j and \mathbf{x}_i^s .

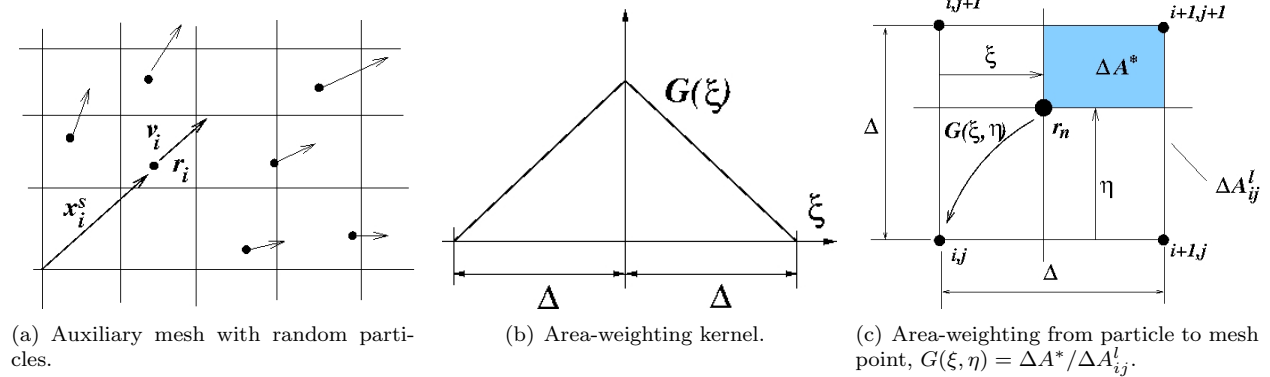


Figure 2. Random particles on mesh and area-weighting, ΔA_{ij}^l denotes the cell area related to the lower left point ij .

C. Enhanced numerical discretization

To significantly increase the numerical efficiency of the general numerical procedure outlined in the previous section, some further algorithmic improvements are introduced, which will be discussed in the following section.

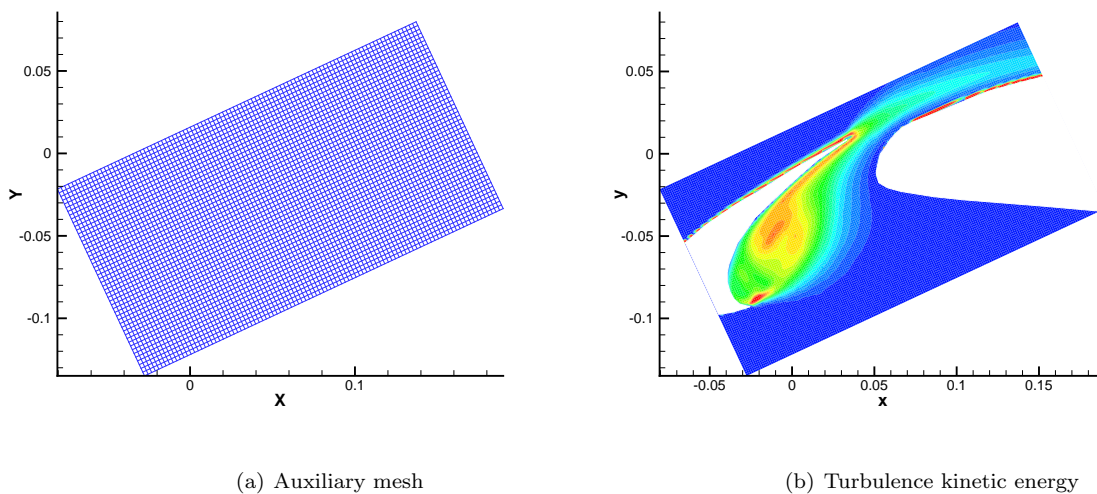


Figure 3. Auxiliary 100×200 Cartesian mesh to resolve acoustic source in the slat-cove and turbulence kinetic energy distribution.

In principle, based on the white-noise representation via random particles, fluctuating quantities on a computational mesh could be directly achieved by distributing the random values with an appropriate filter kernels onto the computational mesh, eq. (12). However, typically each particle contributes to some 100 or

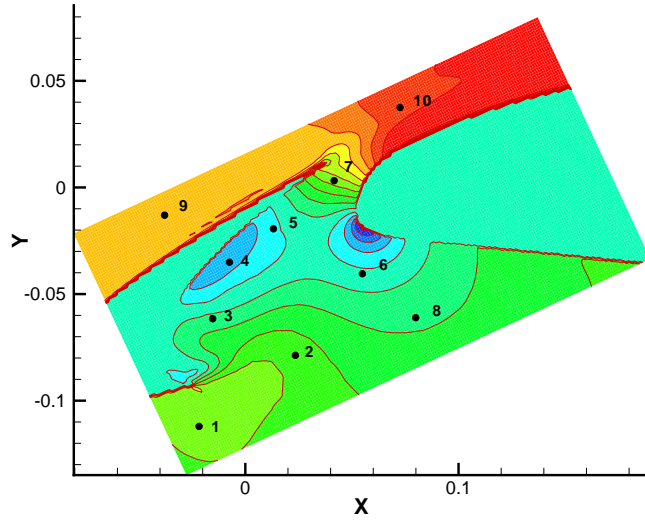


Figure 4. Spatial extension of the auxiliary 100×200 Cartesian grid to resolve acoustic source in the slat-cove and location of discrete sample points.

1000 surrounding mesh points in 2D and 3D, respectively. Therefore, a cheaper alternative is considered here, where the random values are interpolated in an intermediate step with an area-weight particle shape function onto the neighbor mesh points of an auxiliary mesh, Fig. 2. The single-block mesh determines the resolved source region. Since we just consider filter kernels that follow from tensor products, the spatial filtering can be achieved through a sequence of 1D filter operations on the auxiliary mesh, each typically involving some 10 mesh points. Hence, the computational effort to filter the data roughly reduces to 20% in 2D and 3% in 3D compared to a direct method.

In a final step, the fluctuating source data is interpolated onto the final computational grid. From the auxiliary Cartesian mesh, a high-order Hermite interpolation onto a block structured or unstructured CAA mesh point is efficiently achieved using filtered quantities and derivatives of it in neighboring auxiliary mesh points. Some other advantages of an intermediate source mesh are:

- the evaluation of source terms often needs some further derivatives of fluctuating quantities, which can be easily provided through CAA finite-difference schemes on the Cartesian mesh, and in particular simplifies the application of the method in conjunction with unstructured CAA methods
- using the mean-flow field interpolated onto the Cartesian mesh, the propagation of particles can be computed conveniently with sufficient accuracy by mapping the local flow velocity from the surrounding hosting cell corners to the particle location

The area-weighting kernel used to interpolate from the particle to the intermediate mesh and vice versa, reads

$$\mathcal{G}(x) = \begin{cases} 1 - \frac{|x|}{\Delta} & \text{for } |x| \leq \Delta \\ 0 & \text{for } |x| > \Delta \end{cases} \quad (18)$$

Its support is limited through the auxiliary mesh spacing Δ to the immediate mesh neighbors. The applied 2D filter kernel follows from this definition to be $G(x, y) = \hat{A}\mathcal{G}(x)\mathcal{G}(y)$, where the amplitude \hat{A} still has to be defined. With the help of this filter kernel the random values of the discrete particles are interpolated onto the auxiliary mesh such that a discrete approximation to the convective white-noise field \mathcal{W} is realized in each mesh node. This is accomplished if the mean-square value in each mesh node ij is $\overline{\mathcal{W}_{ij}^2} = \Delta A_{ij}$, where ΔA_{ij} denotes the node centered control volume related to point ij . Then the filtered field can be achieved

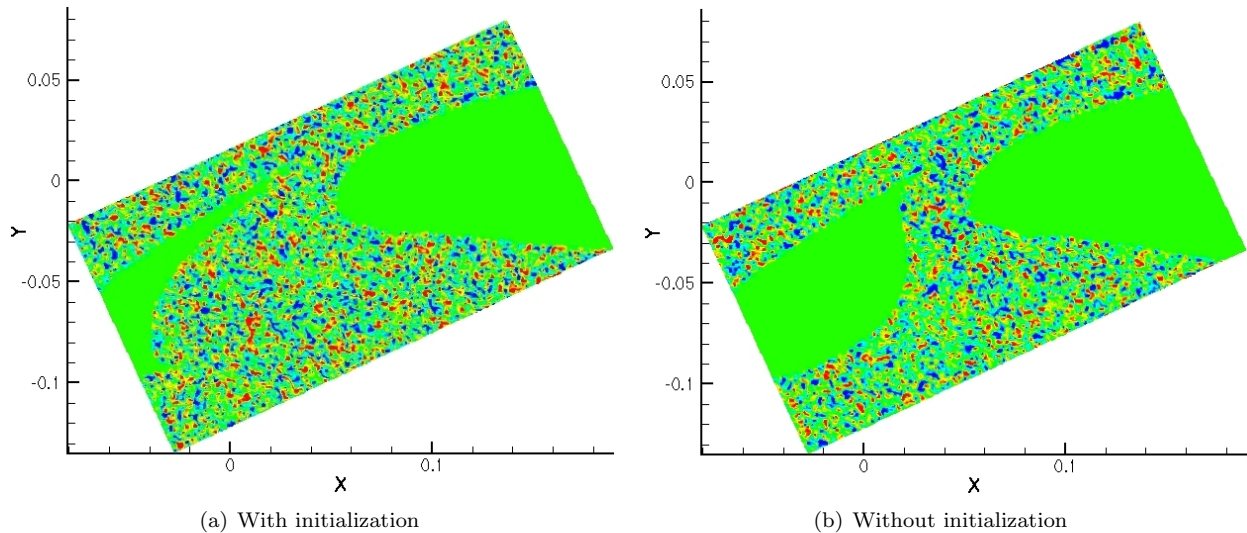


Figure 5. Snapshot of numerical realized white-noise on the 100×200 auxiliary source mesh.

by applying filter stencils of the form

$$\psi_i = \sum_{j=-N}^N d_j \mathcal{W}_j \quad (19)$$

along the grid lines, with the filter coefficients d_j determined by the appropriate spatial filter kernel to achieve a desired correlation function, evaluated for locations i and j .

The area-weight kernel eq. (18), which is applied in the first step to interpolate from the random particles to the mesh nodes, can be interpreted as a special choice of a filter kernel in eq. (6) as well, if the discrete particles realize a sufficient good approximation to the white-noise field defined by eqs. (3-5) on the length scale of the auxiliary mesh cell. The necessary number of particles per cell were determined by numerical experiments and the values achieved will be discussed below. Assuming a sufficient large number of particles used, each represents again the ideal white-noise field eqs. (3-5) for a surrounding volume ΔA_n , which is determined by the local particle density ρ_n , i.e. $\Delta A_n = 1/\rho_n$. The particle density can be achieved in the mesh nodes by summing up the area-weight contribution of all particles to their neighbor mesh points. These values divided by the node centered control volume ΔA_{ij} yields the particle density in the considered mesh point. Hence, the approximated white noise field on the auxiliary mesh, i.e. \mathcal{W} , follows by interpolating the random values times $\sqrt{\rho_n^{-1}}$ with the area-weight kernel onto the auxiliary mesh and by weighting these values with the amplitude \hat{A} .

To achieve a mean-square value of $\Delta A_{ij} = \Delta^2$ of \mathcal{W} in a computational node of the source mesh, the amplitude has to be scaled such that the equality

$$\mathcal{R}(\mathbf{r} = 0, 0) = \overline{\mathcal{W}^2} = \hat{A}^2 \iint \mathcal{G}^2(x') \mathcal{G}^2(y') dx' dy' = \Delta A_{ij}$$

holds. For the area-weighting kernel this yields $\hat{A} = 3/2$.

As a numerical test problem for the previously outlined algorithm, the sound generation at the slat of a high-lift airfoil is considered. Fig. 3(b) shows the turbulence kinetic energy on the source patch defined by the auxiliary grid. Random particles are seeded equally distributed over the source domain not occupied by the geometry. Note that no special treatment at surfaces is necessary. In principle, random values could also be distributed over the interior of geometries. However, if the mean-flow is set to zero in the interior, these interior values will, according to the RPM modeling of convection velocities, only contribute with non-convecting fluctuations to exterior nodes. From Mach number scaling laws, it is known that non-convecting sources will not generate sound. Hence, the contribution of interior values can be omitted if acoustic sources are realized. During run-time convecting particles that leave the source domain are substituted by new random particles seeded at the upstream boundary. Fig. 5 shows the white-noise field \mathcal{W} , which is realized

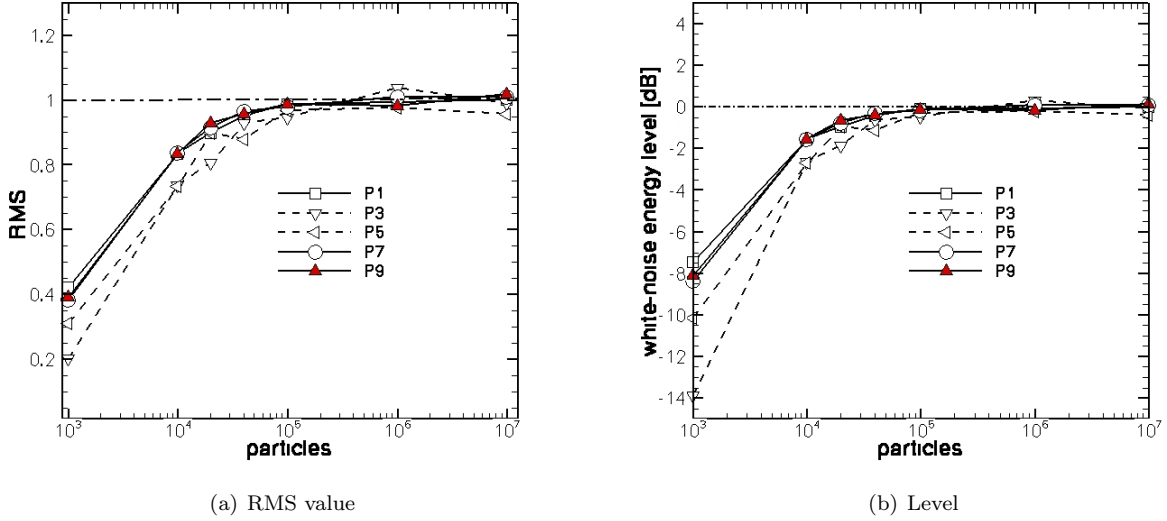


Figure 6. RMS values and levels of fluctuating quantity showing convergence of discrete convective white-noise in the 5 observer points of Fig. 4 (every other observer point shown).

on the auxiliary mesh. If the full flow field in the source domain is initialized with random particles, also recirculation regions e.g. in the slat cove can be resolved, Fig. 5(a). If particles are only seeded over the inflow boundary without initialization, recirculation regions can be excluded, Fig. 5(b).

RMS values and energy levels of the approximated white-noise field \mathcal{W} on the auxiliary mesh, which are normalized with $\sqrt{\Delta A_{ij}}$ are depicted in Fig. 6 for 5 observer points according to Fig. 4, using different numbers of random particles. The dashed lines in the Fig. 6 correspond to observer positions lying in the recirculatory region of the slat cove. It is evident that using an adequate number of particles, ($n \geq 10^5$), the target value $\overline{\mathcal{W}^2}/\Delta A_{ij} = 1$ can be reached very accurately for all test points on the source mesh. The lowest number of necessary particles (10^5 particles) corresponds to approximately 5 particles-per-cell (PPC). To achieve RMS values with similar good quality in the recirculation domain, at initializing time particles have to be equally distributed throughout the domain such that the particle density is as much as possible homogeneous. Furthermore, the particles have to be appropriately seeded at the inflow boundaries during run-time to avoid a drift in the particle density in the flow domain affected by the incoming mean-flow. Apparently, the convergence is slightly weaker for points in the recirculation bubble, however, a ratio of 5 PPC is also sufficient for these points to closely reach a normalized target RMS value of one.

According to eq. (7), the auto-convolution of $G(x, y)$ yields the correlation function of the induced fluctuating field. For the considered area-weight kernel, the resulting correlation function is composed out of a sequence of one-dimensional kernels, i.e., $R(x, y) = r(x/\Delta)r(y/\Delta)$. The one-dimensional kernels can be found from the convolution of the kernel eq. (18) to be

$$r(\xi) = \begin{cases} 1 - \frac{3}{2}\xi^2 + \frac{3}{4}\xi^3 & \text{for } |\xi| < 1 \\ \frac{1}{4}(2-x)^3 & \text{for } 1 \leq |\xi| < 2 \\ 0 & \text{for } 2 \leq |\xi| \end{cases} . \quad (20)$$

This kernel is well known in the literature as a cubic spline approximation to a Gaussian with limited support. According to the properties of a Gaussian, the kernel exhibits approximately isotropy, i.e. it is a pure function of radial distance $r = \sqrt{x^2 + y^2}$, $R(x, y) \simeq R(r)$. Form eq. (20) the integral length scale,

$$l_t = \int_0^\infty r(\xi)d\xi, \quad (21)$$

follows to be $l_t = 3/4\Delta$. Compared to an exact Gaussian, the cubic-spline approximation has the advantage

- to have a limited support, i.e. filter stencils are strictly limited,

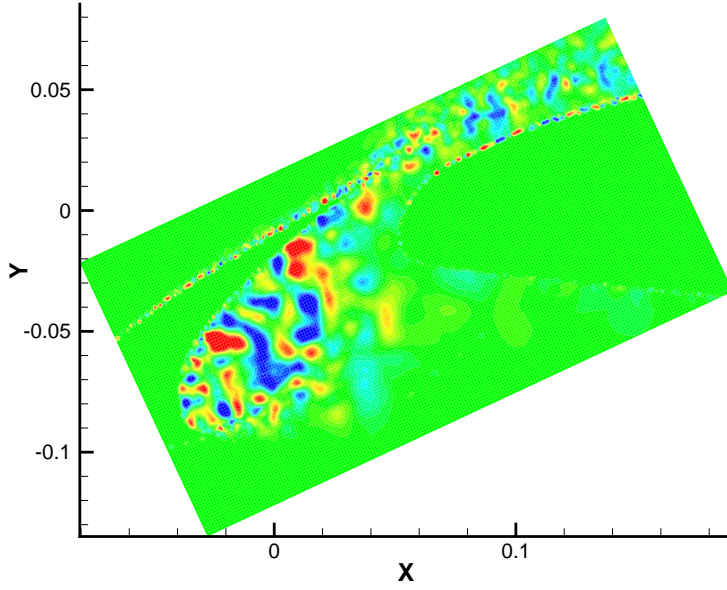


Figure 7. Slat noise source with full resolved slat-cove, $c_l = 0.54$, eq. (30).

- and to be generated by a filter kernel, i.e. eq. (18), which is computationally very efficient.

Fig. 7 shows a snapshot of the filtered source field in the slat cove using an area-weight to filter on the auxiliary mesh and resolving the slat cove region through initialized random particles.

The spectral density of a single-sided, wave-number based PSD at zero wave-number is related to the correlation function $f(r)$ through

$$E_1(k = 0) = \frac{2}{\pi} \frac{\overline{u^2}}{u^2} \int_0^\infty f(r) dr = \frac{2}{\pi} \overline{u^2} l_t,$$

where l_t denotes the integral length scale. Hence, to yield a unity spectrum in the resolved range, the nodal fluctuations, whose energy is normalized to unity, must be normalized with $(\frac{3}{2\pi} \Delta)^{-1}$. Such normalized spectral levels are depicted in Fig. 10 for different numbers of particles applied. It is evident that using an adequate number of particles, a unity spectrum can be achieved with good accuracy in the resolved regime up to the Nyquist cut-off limit of the auxiliary mesh. The red lines in the graph indicate the Nyquist wave-number π/Δ of the mesh. The spectra are obtained from the time-signal in 10 test points on the mesh. Using the local mean-flow velocity in the respective mesh points, the frequency spectra are rescaled in terms of wave-numbers. It is evident that independent of the actual flow velocity and direction in the considered mesh points, all spectra collapse almost perfectly to one common shape. This implies two things, namely, that the convection property of the discrete white-noise realization is indeed satisfied and that the effective correlation function is almost isotropic.

Again, dashed lines indicate the points lying in the recirculation bubble of the test problem. For 10^5 particles, which yields 5 PPC, a converged status is achieved with a level difference to the target value less than 1dB. From the Fig. 10 it is further evident that similar spectra and spectral densities can be maintained in the recirculation bubble during run-time.

Fig. 11 presents the spatial correlation function for the 10 test points. The spatial correlations are determined from the temporal correlations in the considered points, scaled with the local mean-flow velocity. Note that the spatial coordinate in Fig. 11 is scaled in addition with the mesh resolution Δ . Again, independent of the local mean-flow direction, all spatial correlations collapse to one common shape-function and shows

very good agreement with the theoretical cubic spline correlation, eq. (20). In Fig. 11(d) the PSDs related to the cubic spline and a Gaussian correlation, the latter with length-scale $3/4\Delta$, are included into the graph. Very good agreement between the cubic spline correlation and the simulated PSDs is evident in all 10 points. Since the cubic spline approximates a Gaussian, their spectral shape agree for a wide range of wave-numbers. Only at higher wave-numbers, beyond the Nyquist limit of the mesh, some derivations occur.

D. Sound sources from modeled turbulent velocities

One approach to realize acoustic sound sources is to model turbulent velocities as a basis to determine vortex sound sources. For example, the major vortex sound contribution to the Lighthill tensor is the term $\rho u_i u_j$. To model turbulent related velocities with the RPM method the divergence-free conditions of vorticity related turbulence is taken into account by identifying the modeled fluctuating quantity with a streamfunction $\psi(\mathbf{y}, t)$. Strictly solenoidal 2D perturbation velocities are deduced from this fluctuating streamfunction at each time instant via

$$u_i = \epsilon_{ij} \frac{\partial \psi}{\partial y_j}, \quad (22)$$

where ϵ_{ij} denotes the 2D ϵ -tensor. In case of homogeneous isotropic turbulence the velocity correlations that follow from eq. (22),

$$\mathcal{R}_{ij}(\mathbf{r}, \tau) = \overline{u_i(\mathbf{r}_1, t_1) u_j(\mathbf{r}_2, t_2)}, \quad (23)$$

match perfectly the complete velocity correlation tensor of isotropic turbulence for $\tau = 0$,

$$\mathcal{R}_{ij}(\mathbf{r}, 0) = \frac{2}{3} \bar{k} \left[\frac{f(r) - g(r)}{r^2} r_i r_j + g(r) \delta_{ij} \right]. \quad (24)$$

In the above expressions $\mathbf{r} = \mathbf{r}_1 - \mathbf{r}_2$ and $\tau = |t_1 - t_2|$ are the spatial and temporal separations between point 1 and 2. The separation distance is $r = |\mathbf{r}|$ and r_i is the i th component of vector \mathbf{r} . The turbulence kinetic energy is denoted by \bar{k} and $f(r)$ and $g(r)$ denote the longitudinal and lateral correlation functions, respectively, which are connected for a two-dimensional problem through

$$g(r) = f(r) + r \frac{df(r)}{dr}. \quad (25)$$

This neat feature to exactly realize homogeneous isotropic turbulence in the two-point correlations can be proven by considering the space-time correlations of the fluctuating streamfunction in this homogeneous case to be a pure function of the separation vector \mathbf{r}

$$\mathcal{R}_{\psi\psi}(\mathbf{r}, \tau) = \overline{\psi(\mathbf{r}_1, t_1) \psi(\mathbf{r}_2, t_2)}. \quad (26)$$

The velocity correlations eq. (23) are connected via eq. (22) with the correlations eq. (26). By taking $\mathbf{r} = \mathbf{r}_1 - \mathbf{r}_2$ into account, the relationship is

$$\mathcal{R}_{ij} = -\epsilon_{ik} \epsilon_{jl} \frac{\partial^2 \mathcal{R}_{\psi\psi}}{\partial r_k \partial r_l}. \quad (27)$$

Since ψ is generated by a procedure that realizes correlations of the type described by eq. (1), the correlation $\mathcal{R}_{\psi\psi}$ in eq. (27) can be expressed through the right-hand side of eq. (1), where the parameters are constants for the homogeneous problem. Next, the explicit expressions found for \mathcal{R}_{ij} in the case $\tau = 0$ can be verified to have the formal shape defined by eq. (24), whereby the resulting longitudinal and lateral correlation functions furthermore satisfy eq. (25). To match quantitatively eq. (24) the amplitude \hat{R} in eq. (1) has to set to

$$\hat{R} = \frac{4l_s^2 \bar{k}}{3\pi}. \quad (28)$$

Then, the resulting longitudinal correlation function that follows from eq. (1) is a Gaussian,

$$f(r) = \exp\left(-\frac{\pi}{4} \frac{r^2}{l_s^2}\right), \quad (29)$$

with an integral length scale directly determined by the parameter l_s ,

$$L = \int_0^\infty f(r)dr = l_s.$$

Hence, the parameters \hat{R} and l_s in eq. (1) are directly linked via eqs. (28) and (29) to the turbulence kinetic energy and length scale as provided by RANS. One free empirical constant c_l has to be determined, which defines the relation between the RANS length scale and the integral length scale of turbulence. For a $k - \epsilon$ turbulence model the relation is

$$l_s = c_l \frac{\bar{k}^{3/2}}{\epsilon}. \quad (30)$$

For a $k - \omega$ model the corresponding relation becomes

$$l_s = \frac{c_l}{C_\mu} \frac{\bar{k}^{1/2}}{\omega} \quad (31)$$

Following the discussion of Bailly and Juvé⁵ the constant can be estimated to be $c_l \approx 0.54$ for a modified von Karman spectrum. Hence, with $C_\mu = 0.09$, the constant can be estimated with $\frac{c_l}{C_\mu} \approx 6.0$ for the $k - \omega$ -model.

A certain value of \hat{R} in eq. (1) can be achieved, if \hat{A} in eq. (2) is chosen appropriately. Explicit expressions for \hat{A} can be found in Ref.⁴ The approach eq. (22) can be extended to 3D, details can be found in Ref.⁴ as well.

E. Time domain realization of Tam & Auriaults jet-noise source

The statistical jet noise model of Tam & Auriault¹ is based on the modified linearized Euler equations rewritten in cylindrical coordinates as governing acoustic equations. The modifications include the neglect of jet spreading terms as well as mean-flow gradients. Through the mean-flow gradients the continuity equation is coupled with the momentum equations. In the Tam & Auriault model the continuity equation is not used since it decouples from the momentum equation if mean-flow gradients are not considered. Furthermore, an acoustic source term is introduced on the right-hand side of the momentum equation. In Cartesian coordinates and including the jet spreading terms (i.e. only with the mean-flow gradients omitted), their governing equations read

$$\rho_0 \left[\frac{\partial \mathbf{u}'}{\partial t} + \mathbf{u}_0 \nabla \mathbf{u}' \right] + \nabla p = -\nabla q_s \quad (32)$$

$$\frac{\partial p}{\partial t} + \mathbf{u}_0 \nabla p + \gamma p_0 \nabla \cdot \mathbf{u}' = 0. \quad (33)$$

In a next step Tam & Auriault use the adjoint equations to the frequency domain Fourier transform of eqs. (32,33) to derive expression for the free-space Green's functions of the governing equations (32,33) in the frequency domain. The Green's functions include mean-flow refraction effects and have been computed with CAA techniques. Finally, the numerically determined values of the Green's function are used to approximately solve the integral expression that defines the far-field acoustic spectrum in terms of the noise source space-time correlation

$$\left\langle \frac{D_0 q_s(\mathbf{x}_1, t_1)}{Dt_1} \frac{D_0 q_s(\mathbf{x}_2, t_2)}{Dt_2} \right\rangle. \quad (34)$$

In the above expression $D_0/Dt := \partial/\partial t + \mathbf{u}_0 \cdot \nabla$ denotes a substantial time derivative and the brackets indicate an ensemble average. Tam & Auriault propose the correlation function eq. (34) to be described by

$$\left\langle \frac{D_0 q_s(\mathbf{x}_1, t_1)}{Dt_1} \frac{D_0 q_s(\mathbf{x}_2, t_2)}{Dt_2} \right\rangle = \frac{\hat{q}_s^2}{c^2 \tau_s^2} \times \exp \left\{ -\frac{|\xi|}{u_0 \tau_s} - \frac{\ln 2}{\hat{l}_s^2} [(\xi - u_0 \tau)^2 + \eta^2 + \zeta^2] \right\}. \quad (35)$$

Note that the above correlation function considers a mean-flow in x -direction, i.e. only the velocity component u_0 is non-zero. This condition is approximately satisfied for a slightly spreading jet. Furthermore, the ratio $|\xi|/u_0$ of separation distance between point 1 and 2 and local convection velocity could be expressed through the time separation $|\tau|$ as well.

To model the noise source with the fast RPM method in the time-domain the initial equation system eqs. (32,33) has to be reformulated. That is, the pressure is decomposed according to

$$p := p' - q_s, \quad (36)$$

respectively $p' = p + q_s$. Since q_s was introduced by Tam & Auriault as a turbulence related pressure fluctuation, the meaning of the decomposition eq. (36) is that p' is a perturbation pressure with all turbulence related pressure fluctuations included, whereas p in eqs. (32,33) is a fluctuating pressure, which excludes the turbulence related pressure fluctuations. Note that p' as well as p comprise all relevant acoustic pressure fluctuations. Next, by introducing the decomposition eq. (36) into eqs. (32,33) the modified equation system that follows reads

$$\rho_0 \left[\frac{\partial \mathbf{u}'}{\partial t} + \mathbf{u}_0 \nabla \mathbf{u}' \right] + \nabla p' = 0 \quad (37)$$

$$\frac{\partial p'}{\partial t} + \mathbf{u}_0 \nabla p' + \gamma p_0 \nabla \cdot \mathbf{u}' = \frac{D_0 q_s}{Dt}. \quad (38)$$

In this reformulation of the governing perturbation equations the scalar source term $D_0 q_s / Dt$ appears on the left-hand side of the pressure equation. The correlation of this scalar quantity can be modeled with the RPM method, which becomes evident by comparing the correlation eq. (35) with that realized by the RPM method, eq. (1). It can be identified that the turbulent length-scales l_s in eq. (1) and \hat{l}_s in eq. (35) are related through

$$l_s = \frac{1}{2} \sqrt{\frac{\pi}{\ln(2)}} \hat{l}_s. \quad (39)$$

Tam & Auriault propose to model the length scale as $\hat{l}_s = \hat{c}_l k^{3/2} / \epsilon$, with $\hat{c}_l = 0.256$. This yields

$$l_s = c_l \frac{k^{3/2}}{\epsilon}, \quad (40)$$

with $c_l = 0.273$. Note that the turbulent pressure, whose correlations are modeled here, is a function of the turbulent velocities squared. Interestingly, a value of $c_l = 0.273$ is exactly half as large as the parameter found for the velocity correlations, eq. (30).

As an extension of the statistical source description, the restriction of having only a non-zero velocity component u_0 along the jet axis can be dropped in the framework of the RPM model in favor of a full use of the mean-flow from RANS. In the applications discussed so far the modeled fluctuating quantity ψ is used as a streamfunction, from which solenoidal turbulent velocity components are derived subsequently. The turbulent velocities serve as a basis to compute velocity dependent sound sources. In contrast, the extension for a primal Tam & Auriault approach in the time-domain mainly means to generate the scalar source $D_0 q_s / Dt$ by directly identifying it with the fluctuating quantity ψ provided by the RPM model. For this, the amplitude \hat{A} in eq. (2) has to be chosen such that a value \hat{R} in eq. (1) is realized, which satisfies

$$\hat{R} = \frac{\hat{q}_s^2}{c^2 \tau_s^2}. \quad (41)$$

More details about scaling \hat{A} can be found in Refs.^{3,4}

The generation of fluctuations with the RPM method was discussed so far for frozen turbulence, having Gaussian spatial correlations and involving Taylor's hypothesis. The simulation of frozen turbulence is found to be sufficient for the modeling of airframe noise mechanisms. To simulate jet-noise, however, the realization of proper time correlations, using local time-scales, is deemed crucial, since it is the change in turbulence that is responsible for jet-noise generation. To include the exponential time decay of eq. (1), eq. (5) has to be extended to a Langevin equation. In the numerical realization this means that the random values carried by each particle are not constant but rather change over time according to the discrete equation

$$r_i^{n+1} = \alpha r_i^n + \beta s_i^n. \quad (42)$$

Here r_i^{n+1} and r_i^n denote the random value of a particle at time-level $n+1$ and n , respectively. The quantity s_i^n is a new random value in the same range as r_i . This procedure realizes an exponential decay, Ref.⁶ The constant α is related to the time-scale τ_s via

$$\alpha = \exp\left(-\frac{\Delta t}{\tau_s}\right), \quad (43)$$

where Δt denotes the time-increment between levels $n + 1$ and n . To preserve the root-mean square value of r_i over time, β is related to α via $\beta = \sqrt{1 - \alpha^2}$.

III. Sample results

A. Flat-plate trailing edge noise

Preliminary results for the sound generated at the trailing-edge of an infinite thin flat plate at $M = 0.11$ are presented in Fig. 12. The results are obtained with the DLR CAA solver PIANO,⁷ utilizing the RPM model. Fig. 12(a) is a snapshot of the sound field, showing the typical wave pattern of sound waves generated at the trailing edge. Fig. 12(b) presents directivities for a circle centered at the trailing edge, having a radius $r = 1.5l$, with l denoting the chord length. The directivity patterns for wave-numbers $kl = 5, 10, 15$ correspond very well to those discussed by Howe.⁸ The narrow band spectrum $1.5l$ above the trailing edge, Fig. 12(c), shows a low-frequency maximum and falls off to higher frequencies. This general shape corresponds to that known from measurements, see e.g. Yu & Tam.⁹ The RPM based trailing edge characteristics will be analyzed further in comparison with experiments as part of the ongoing work.

B. Jet noise with the primal Tam & Auriault approach

This section reports first results for the Tam & Auriault jet noise approach solved in the time-domain. Fig. 13(a) presents the turbulence kinetic energy distribution of the considered jet problem. However, according to the Tam & Auriault model, the relevant source quantity is the turbulence dissipation rate, since the root-mean square of the source term is equal to $\hat{q}_s/c\tau_s$, eq. (35). This term is proportional to $\rho_o\epsilon$, with ϵ being the turbulent dissipation rate. The corresponding field is shown in Fig. 13(b). It is evident that two source regions are present. One is related to the region of maximal turbulence kinetic energy. Another region, however, is located in the shear layer downstream of the nozzle. Fig. 14 shows the radiated sound field based on the Tam & Auriault source term, using the linearized Euler equations with all mean-flow gradients omitted, Fig. 14(a), and using the full LEE set, Fig. 14(b). It is evident that the full set of equations, which includes hydrodynamic instabilities, gives a distinct radiation lobe for angles around 50° from the jet axis. Although such a pattern is well known from high-fidelity simulations such as LES or DES, it has to be checked further, whether these instability related wave amplitudes are matched also quantitatively well using linearized equations. Note that these distinct lobes are missing in the original Tam & Auriault approach as well, since the adjoint equations neglect the mean-flow gradients. The directivity that occurs without mean-flow gradients is shown in Fig. 14(a). However, under 90° angle from the jet axis the spectra obtained with the full LEE and with the LEE without mean-flow gradients match quite well, Fig. 15.

C. Slat Noise: Scaling law and effect of slat-cove cover

The effect of a slat cove cover on the radiated sound field is studied. Fig. 16 shows the geometry of the slat cove cover and the topology of the CAA mesh in the vicinity of the slat. Fig. 17 juxtaposes a snapshot of the acoustic field for the clean slat (left) to that involving the slat cove cover (right). Since the pressure contour scaling was kept constant in both cases, it is evident from the field plots that the slat cove cover achieves a decrease in the acoustic amplitudes. This effect is also highlighted by comparing the narrow band spectra for an observer position 1.5 clean chord lengths beneath ($\theta = 270^\circ$) the slat for two different velocities (30m/s, 56m/s), Fig. 18. In average a decrease of the sound pressure levels around $5dB$ is found for frequencies up to $8kHz$ for the lower velocity.

Results of a Mach number scaling study are plotted in Fig. 19. Three different Mach numbers (0.088, 0.12, 0.16) are considered. From experiments it is deduced that the sound intensities scale according to a $M^{4.5}$ law for slat-noise, i.e., a slightly weaker growth compared to airfoil trailing edge noise, which can be shown analytically to scale with M^5 . Usually the exponent can be attributed to several effects. First, the change of the convection velocity of vortical structures causes an increase in the radiated sound pressure. Second, the turbulent velocity fluctuations grow with increasing flow velocity. For analytical considerations it is usually assumed that the turbulent velocity fluctuation scale linearly with the freestream velocity. In the stochastic model the convection property is accounted for by convecting the random particles in the steady RANS mean-flow. The increase of turbulent fluctuations is taken into account in the model by the change of the turbulence kinetic energy levels, which are provided by the steady RANS solution. The Fig. 19 depicts the

scaling of the root-mean square (RMS) fluctuating pressure for an observer position 1.5c below $\theta = 270^\circ$ and above $\theta = 90^\circ$ the slat trailing edge. The three data points yield a Mach number scaling law exponent between 1.51 and 1.75 for RMS pressure. Since the sound intensities scale with twice that value, one finds a scaling law with exponents between 3.02 and 3.5 for the considered 2D case. In^{10,11} it was discussed that a 2D acoustic solution has to be corrected to take into account 3D sound radiation, which increases the scaling exponent by one. The correction formula in can be written as

$$\tilde{p}(0, R, \theta, \omega) \simeq \hat{p}(R, \theta, \omega) \frac{1+i}{2} \sqrt{\frac{kL^2}{\pi R}}. \quad (44)$$

Here \tilde{p} denotes the 3D corrected (complex) spectral pressure and \hat{p} is related to the 2D spectral pressure. L denotes a length scale of the problem, see Ref.¹² Based on Taylor's hypothesis of convecting vorticity, the non-dimensionalizing of Eq. (44) yields with $k = \omega/c$, $\omega \propto u/\lambda_v$, where λ_v is the length scale of a vortical disturbance, the scaling

$$\tilde{p} \propto M^{1/2} \hat{p},$$

i.e., the sound intensities in 3D scale with the power of the Mach number increased by one, compared to the 2D case. Accordingly, the corrected 3D scaling becomes 4.02 and 4.5, respectively, which is pretty close to the expected exponent.

IV. Summary & Conclusion

The generation of synthetic fluctuations that realize Gaussian spatial and exponential temporal correlations with locally varying integral length- and time-scales, as well as turbulence kinetic energy was discussed. It was shown that using a particle density exceeding 5 particles per mesh cell, an approximation of white-noise can be achieved very accurately up to the Nyquist wave-number on a discrete mesh. The white-noise field is needed to set up synthetic fluctuations with the desired correlations in a second step through spatial filtering. The time-domain realization of Tam & Auriault's jet noise source for a primal time-domain CAA approach was discussed. Sample results for trailing edge noise, jet noise, and high-lift noise were presented. The Mach number scaling law for slat noise closely approaches the values known from experiment. The noise reducing effect of a slat cove filler could be predicted.

References

- ¹Tam, C. and Auriault, L., "Jet Mixing Noise from Fine-Scale Turbulence," *AIAA Journal*, Vol. 37(2), 1999, pp. 145–153.
- ²Ewert, R. and Emunds, R., "CAA Slat Noise Studies Applying Stochastic Sound Sources Based On Solenoidal Digital Filters," *AIAA Pap. 2005-2862*, 2005.
- ³Ewert, R., "Slat Noise Trend Predictions Using CAA With Stochastic Sound Sources From A Random Particle-Mesh Method (RPM)," *AIAA Pap. 2006-2667*, 2006.
- ⁴Ewert, R., "Broadband Slat Noise Prediction based on CAA and Stochastic Sound Sources from a Random Particle-Mesh (RPM) method," *in press Comp.and Fluids*, 2007.
- ⁵Bailly, C. and Juve, D., "A Stochastic Approach To Compute Subsonic Noise Using Linearized Euler's Equations," *AIAA Pap. 99-1872*, 1999.
- ⁶Billson, M., Erikson, L.-E., and Davidson, L., "Modelling of Synthetic Anisotropic Turbulence and Its Sound Emission," *AIAA Pap. 2004-2857*, 2004.
- ⁷Delfs, J., Bauer, M., Ewert, R., Grogger, H., Lummer, M., and Lauke, T., "Numerical Simulation of Aerodynamic Noise with DLR's aeroacoustics code PIANO," Tech. rep., DLR, PIANO manual for version 5.1, 2007.
- ⁸Howe, M., "Edge-source Green's function for an airfoil of arbitrary chord, with applications to trailing edge noise," *Q. Jl. Mech. Appl. Math.*, Vol. 54(1), 2001, pp. 139–155.
- ⁹Yu, J. and Tam, C., "Experimental Investigation of the Trailing Edge Noise Mechanism," *AIAA Journal*, Vol. 16(9), 1978, pp. 1046–1052.
- ¹⁰Oberai, A., Roknaldin, F., and Hughes, T., "Computation of Trailing-Edge Noise Due to Turbulent Flow over an Airfoil," *AIAA Journal*, Vol. 40/11, 2002, pp. 2206–2216.
- ¹¹Ewert, R., Zhang, Q., Schröder, W., and Delfs, J., "Computation of Trailing Edge Noise of a 3D Lifting Airfoil in Turbulent Subsonic Flow," *AIAA Pap. 2003-3114*, 2003.
- ¹²Ewert, R. and Schröder, W., "Acoustic Perturbation Equations Based on Flow Decomposition via Source Filtering," *J. Comput. Phys.*, Vol. 188, 2003, pp. 365–398.
- ¹³Crighton, D., Dowling, A., Williams, J. F., Heckl, M., and Leppington, F., *Modern Methods in Analytical Acoustics*, Springer-Verlag New York Berlin Heidelberg, 1992.

Appendix

A. Consistency of the filter integral approximation

To show the integral approximation to be fourth order accurate, rewrite eq. (2) using an averaged white-noise field $\langle \mathcal{U}_i \rangle$ instead of \mathcal{U}_i

$$\psi(\mathbf{x}, t) = \sum_{i=1}^M \int_{\Delta A_i} G(\mathbf{x}, \mathbf{x}') \langle \mathcal{U}_i \rangle d\mathbf{x}' = \sum_{i=1}^M \langle \mathcal{U}_i \rangle \int_{\Delta A_i} G(\mathbf{x}, \mathbf{x}') d\mathbf{x}'. \quad (45)$$

Now, inserting a Taylor expansion of the kernel around \mathbf{x}_i^s , i.e. $G' = G_i + \nabla G_i \cdot (\mathbf{x}' - \mathbf{x}_i^s) + \mathcal{O}(h^2)$ (with $G_i := G(\mathbf{x}, \mathbf{x}_i^s)$, $G' := G(\mathbf{x}, \mathbf{x}')$, and $h^2 \propto \Delta A_i$), and using the definition eq. (13), it follows

$$\psi(\mathbf{x}, t) = \sum_{i=1}^M G_i(\mathbf{x}) \langle \mathcal{U}_i \rangle \Delta A_i + \mathcal{O}(h^4).$$

B. Convection velocity of random particles

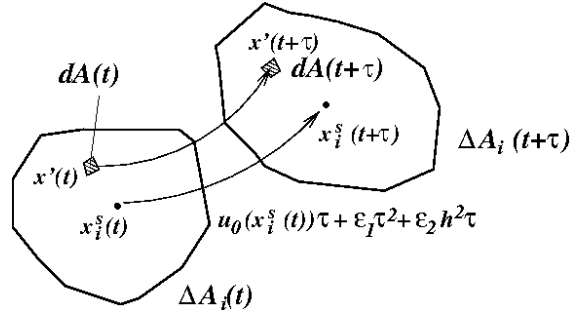


Figure 8. Sketch of one drifting control volume ΔA_i ; ε_1 and ε_2 denote constants that limit the leading temporal and spatiotemporal error terms.

Consider a small element dA in subdomain ΔA_i at initial position $\mathbf{x}'(t)$, Fig. 8. Taylor expansion gives its position a time τ later with $\mathbf{x}'(t+\tau) = \mathbf{x}'(t) + d\mathbf{x}'(t)/dt \cdot \tau + \varepsilon_1 \tau^2$. The element drifts with the mean-flow, i.e. $d\mathbf{x}'/dt = \mathbf{u}_0'$. The velocity \mathbf{u}_0' at \mathbf{x}' follows from a spatial Taylor expansion around the subdomain center \mathbf{x}_i^s : $\mathbf{u}_0' = \mathbf{u}_i^s + \nabla \mathbf{u}_i^s (\mathbf{x}'(t) - \mathbf{x}_i^s(t)) + \varepsilon_2 h^2$ (with $\mathbf{u}_i^s := \mathbf{u}_0(\mathbf{x}_i^s(t))$). Then the cell center location at $t + \tau$ follows by introducing

$$\mathbf{x}'(t+\tau) = \mathbf{x}'(t) + \mathbf{u}_i^s \tau + \nabla \mathbf{u}_i^s (\mathbf{x}'(t) - \mathbf{x}_i^s(t)) \tau + \varepsilon_1 \tau^2 + \varepsilon_2 h^2 \tau$$

into eq. (13). Evaluation of the integral (in incompressible flow dA and ΔA_i are invariants) and differentiation with respect to τ yields the convection velocity eq. (17) of the cell center at time level t (i.e. at $\tau = 0$).

C. Derivation of the convective white-noise field

For the previous derivations a white-noise field was applied with the properties defined by the equations (3-5). It follows from the convection eq. (5) that the properties of the white-noise field in the interior of a considered computational domain are completely prescribed by its properties on the inflow boundary (neglecting at the moment the possible case of closed interior streamlines, e.g., due to recirculation bubbles). Furthermore, eq. (4), which has to be satisfied for each field point in the considered source domain, poses an additional constraint on the white-noise field. I must be verified whether this additional constraint can be realized throughout the computational domain by a convective white-noise field that already fulfills the constraint eq. (5).

Furthermore, although it is clear that the auto-covariance of temporal white-noise yields a δ -function with a time delay as an argument, the occurrence of two spatial δ -functions in eq. (4) as a result of a temporal

average must be clarified. The property of temporal white-noise follows starting with the definition of the Fourier transform

$$\tilde{p}(\omega) = \int_{-\infty}^{\infty} p(t)e^{i\omega t} dt, \quad p(t) = \frac{1}{2\pi} \int_{-\infty}^{\infty} \tilde{p}(\omega)e^{-i\omega t} d\omega. \quad (46)$$

Hence, the auto-covariance $P(\Delta t) = \overline{p(t)p(t + \Delta t)}$ is related to its power spectral density $\tilde{P}(\omega)$ via

$$P(\Delta t) = \frac{1}{2\pi} \int_{-\infty}^{\infty} \tilde{P}(\omega)e^{-i\omega\Delta t} d\omega. \quad (47)$$

For a unity white-noise field $\tilde{P}(\omega) = 1$ this becomes

$$\overline{p(t)p(t + \Delta t)} = \frac{1}{2\pi} \int_{-\infty}^{\infty} e^{-i\omega\Delta t} d\omega = \delta(\Delta t). \quad (48)$$

It will be shown in the following that the constraint imposed by eq. (4) appears as a consequence of the convection property eq. (5). The discussion will specify furthermore how white-noise must be seeded along an inflow boundary to achieve both properties in the considered domain.

As a precursor to the convective white-noise field, lets consider first a spatiotemporal white-noise field with one spatial dimension, $\mathcal{U}(\eta, t)$, which is supposed to realizes the following covariance

$$R(\Delta\eta, \Delta t) = \overline{\mathcal{U}(\eta, t)\mathcal{U}(\eta + \Delta\eta, t + \Delta t)} := \delta(\Delta\eta)\delta(\Delta t). \quad (49)$$

Here $\Delta\eta$ and Δt denote, respectively, the spatial and temporal separation of \mathcal{U} . As discussed, the second δ -function in eq. (49), $\delta(\Delta t)$, is a consequence of a unity white-noise field in the frequency domain.

The additional δ -function on the RHS of eq. (49), $\delta(\Delta\eta)$, indicates that the white-noise fields are independent realizations for all points η , i.e for two non-coinciding points the covariance is zero. However, for independent but otherwise pure temporal white-noise realizations the spatial covariance would rather appear as a Kronecker symbol in eq. (49) with

$$\delta_{\text{K}}(\Delta\eta) = \begin{cases} 0 & \text{for } \Delta\eta \neq 0 \\ 1 & \text{for } \Delta\eta = 0 \end{cases} \quad (50)$$

than as a spatial Dirac function $\delta(\Delta\eta)$. The Dirac delta function can be thought to describe the limit of a discrete realization, where the independent temporal white-noise signals are generated for discrete points $\Delta\eta^*$ apart, with each signal in addition scaled with $(\Delta\eta^*)^{-1/2}$. The spatial delta function in eq. (49) can be deemed to describe the limit $\Delta\eta^* \rightarrow 0$ of these discrete spatiotemporal white-noise realizations.

In a next step a curve $\mathbf{x}_{\text{B}}(\eta)$ with parameter η is introduced. The quantity η can be gauged such that $|\Delta\eta|$ denotes the arc length between two points $\mathbf{x}_{\text{B}}(\eta)$ and $\mathbf{x}_{\text{B}}(\eta + \Delta\eta)$ along the curve. Hence, the covariance eq. (49) can be esteemed as the covariance between the two points on the curve. Furthermore, a steady incompressible two-dimensional mean-flow is introduced through a streamfunction $\psi(\mathbf{x})$,

$$\mathbf{u}_0 = \left(\frac{\partial\psi}{\partial y}, -\frac{\partial\psi}{\partial x} \right)^T. \quad (51)$$

The constraints inherent in this definition of the mean-flow field are introduced at this stage to clarify the subsequent derivation, however poses no bounds on the validity of the method, i.e. with minor modifications, it can be extended to cope further with compressible subsonic mean-flows and three-dimensional problems. The curve \mathbf{x}_{B} is defined to be located orthogonal to the mean-flow velocity vectors, starting in a freely chosen initial upstream position. That is, \mathbf{x}_{B} describes an inflow boundary whereby the gradients $\nabla\psi$ are oriented tangentially to the curve. Furthermore, coordinates ξ can be introduced that give the distance to the curve \mathbf{x}_{B} along the streamlines in upstream direction. With these preparative definitions, see also Fig. 9, a time delay τ can be introduced that gives the time a particle needs to float from a point on $\mathbf{x}_{\text{B}}(\eta)$ to a downstream position $\boldsymbol{\xi} = (\xi, \eta)^T$. Hence, τ is defined by

$$\tau(\xi, \eta) = \int_0^{\xi} \frac{d\xi'}{|\mathbf{u}_0(\xi', \eta)|}. \quad (52)$$

Instead of choosing the previously defined curvilinear coordinates ξ , the time delay could also be expressed in Cartesian coordinates, i.e., $\tau(\mathbf{x})$. It is easy to show that τ is the characteristic solution of the equations

$$u_0 \frac{\partial \tau}{\partial x} + v_0 \frac{\partial \tau}{\partial y} = \mathbf{u}_0 \cdot \nabla \tau = 1, \quad (53)$$

since $\tau = t + t_0$ along the characteristic $d\mathbf{x}/dt = \mathbf{u}_0$. Starting from \mathbf{x}_B with the initial value $t_0 = 0$, this becomes a solution of eq. (52). The convective white-noise field we are seeking for is supposed to satisfy

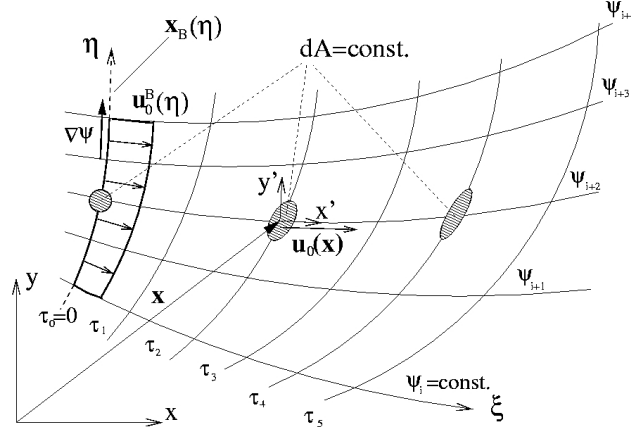


Figure 9. Schematic plot of the quantities used to describe convective white-noise.

$$\frac{D_0 \mathcal{U}^*}{Dt} = \frac{\partial \mathcal{U}^*}{\partial t} + \mathbf{u}_0 \cdot \nabla \mathcal{U}^* = 0. \quad (54)$$

A white-noise field showing this property is realized by introducing the previously defined functions $\psi(\mathbf{x})$ and $\tau(\mathbf{x})$ into eq. (49). To do so, first an auxiliary function with scalar argument has to be defined that satisfies

$$\eta = f(\psi(\mathbf{x}_B(\eta))).$$

Since the curve $\mathbf{x}_B(\eta)$ was defined to be an inflow boundary perpendicular to the local flow velocity, the derivation of both sides with respect to η yields

$$1 = \frac{\partial f}{\partial \psi} \underbrace{\nabla \psi \cdot \frac{d\mathbf{x}_B}{d\eta}}_{\pm u_0^B}. \quad (55)$$

Here u_0^B denotes the mean-flow velocity at the boundary, i.e., $u_0^B(\eta) := u_0(\xi = 0, \eta)$. The sign of u_0^B depends on the definition of the direction of increasing η along \mathbf{x}_B . For example, in Fig. 9 the direction of η would yield a positive sign. Since $u_0^B > 0$ holds for a pure inflow boundary, $\partial f / \partial \psi = \pm (u_0^B)^{-1}$ and f is a strictly monotonic, unique function. Substituting $f(\psi(\mathbf{x}))$ for η and $t - \tau(\mathbf{x})$ for t in eq. (49) the convective white-noise field becomes

$$\mathcal{U}^*(\mathbf{x}, t) = \mathcal{U}(f(\psi(\mathbf{x})), t - \tau(\mathbf{x})). \quad (56)$$

By applying the substantial time derivative D_0/Dt to eq. (56) it is easy to proof eq. (54) to be satisfied, i.e.,

$$\frac{D_0 \mathcal{U}^*}{Dt} = \frac{\partial \mathcal{U}}{\partial t} + \frac{\partial \mathcal{U}}{\partial f} \frac{\partial f}{\partial \psi} \underbrace{\mathbf{u}_0 \cdot \nabla \psi}_{=0, \text{ eq.(51)}} - \frac{\partial \mathcal{U}}{\partial t} \underbrace{\mathbf{u}_0 \cdot \nabla \tau}_{=1, \text{ eq.(53)}} = 0, \quad \text{q.e.d.}$$

It remains to proof that eq. (56) also fulfills eq. (4). With the help of eq. (49) the spatial covariance of eq. (56) becomes

$$\overline{\mathcal{U}^*(\mathbf{x}, t) \mathcal{U}^*(\mathbf{x} + \Delta \mathbf{x}, t)} = \delta(\Delta f) \delta(-\Delta \tau). \quad (57)$$

Due to the properties of the δ -function it is sufficient to express Δf and $\Delta\tau$ in eq. (57) through first-order Taylor expansions, i.e. using eq. (55),

$$\Delta f = \pm(u_0^B)^{-1}\nabla\psi \cdot \Delta\mathbf{x}, \quad (58)$$

$$-\Delta\tau = -\nabla\tau \cdot \Delta\mathbf{x}. \quad (59)$$

To simplify things further, for each point \mathbf{x} in the mean-flow field a local coordinate system $\mathbf{x}' = (x', y')^T$ is introduced, whose x' -axis is aligned with the local mean-flow velocity, and with its origin located at point \mathbf{x} , Fig. 9. The new coordinates are related to $\Delta\mathbf{x}$ through a transformation matrix,

$$\Delta\mathbf{x} = \mathbf{T}\mathbf{x}'. \quad (60)$$

In the new coordinates the eqs. (58,59) become

$$\begin{aligned} \Delta f &= \pm \frac{1}{u_0^B} u_0 y', \\ \Delta\tau &= \frac{1}{u_0} \left(u_0 \frac{\partial\tau}{\partial x'} x' + u_0 \frac{\partial\tau}{\partial y'} y' \right) = \frac{1}{u_0} \left(x' + u_0 \frac{\partial\tau}{\partial y'} y' \right). \end{aligned}$$

In the last step $u_0 \partial\tau / \partial x' = 1$ has been used that follows from eq. (53) and the orientation of the \mathbf{x}' coordinate system. Inserting these expressions for Δf and $\Delta\tau$ into eq. (57) and using the property of the δ -function $\delta(\alpha x) = \delta(x)/|\alpha|$, it follows

$$\overline{\mathcal{U}^*(\mathbf{x}, t) \mathcal{U}^*(\mathbf{x} + \Delta\mathbf{x}, t)} = u_0^B \delta(y') \delta \left(x' + u_0 \frac{\partial\tau}{\partial y'} y' \right). \quad (61)$$

Note that u_0^B in this expression is the inflow velocity at the boundary point related to the field point \mathbf{x} , or fully written $u_0^B(f(\psi(\mathbf{x})))$. This multiplier could be partly removed from the RHS by absorbing it in the boundary white-noise fields of eq. (57), scaling them respectively with $(u_0^B(\mathbf{x}))^{-1/2}$ and $(u_0^B(\mathbf{x} + \Delta\mathbf{x}))^{-1/2}$. Note that taking the value of u_0^B related to point $\mathbf{x} + \Delta\mathbf{x}$ instead of \mathbf{x} means to keep a factor on the RHS. The remaining RHS, with the factor taken into account up to first order, could be reformulated as

$$RHS = \left[1 - \frac{(\nabla u_0^B(\mathbf{x}))^T \mathbf{T}\mathbf{x}'}{2u_0^B(\mathbf{x})} + \dots \right] \delta(\mathbf{d}_1^T \cdot \mathbf{x}') \delta(\mathbf{d}_2^T \cdot \mathbf{x}'), \quad (62)$$

with

$$\mathbf{d}_1 = \begin{pmatrix} 0 \\ 1 \end{pmatrix}, \quad \mathbf{d}_2 = \begin{pmatrix} -1 \\ -u_0 \partial\tau / \partial y' \end{pmatrix}.$$

To show that this RHS is equivalent to that of expression eq. (4) we are seeking for, it is sufficient to proof that eq. (61) exhibits the same integral property as the RHS of eq. (4) for any 'good' test function G , which is

$$\iint_V G(\mathbf{x} - \Delta\mathbf{x}) \delta(\Delta\mathbf{x}) \delta(\Delta y) d\Delta x d\Delta y = G(\mathbf{x}). \quad (63)$$

See e.g. Ref.¹³ for the definition of a 'good' test function. Hence, we have to show

$$\iint_V G(\mathbf{x} - \mathbf{x}') \left[1 - \frac{(\nabla u_0^B)^T \mathbf{T}\mathbf{x}'}{2u_0^B} + \dots \right] \delta(\mathbf{d}_1^T \mathbf{x}') \delta(\mathbf{d}_2^T \mathbf{x}') dV(\mathbf{x}') \stackrel{!}{=} G(\mathbf{x}). \quad (64)$$

Introducing new coordinates $\mathbf{u} = (u, v)^T$ through

$$\begin{pmatrix} u \\ v \end{pmatrix} = \mathbf{D} \begin{pmatrix} x' \\ y' \end{pmatrix}, \quad \mathbf{D} = \begin{pmatrix} \mathbf{d}_1^T \\ \mathbf{d}_2^T \end{pmatrix} = \begin{pmatrix} 0 & 1 \\ -1 & -u_0 \frac{\partial\tau}{\partial y'} \end{pmatrix}, \quad (65)$$

with the inverse transformation given by

$$\begin{pmatrix} x' \\ y' \end{pmatrix} = \mathbf{D}^{-1} \begin{pmatrix} u \\ v \end{pmatrix}, \quad \mathbf{D}^{-1} = \begin{pmatrix} -u_0 \frac{\partial\tau}{\partial y'} & -1 \\ 1 & 0 \end{pmatrix} = \frac{\partial(x', y')}{\partial(u, v)}, \quad (66)$$

the integral of eq. (64) yields

$$\iint_V G(\mathbf{x} - \mathbf{D}^{-1}\mathbf{u}) \left[1 - \frac{(\nabla u_0^B)^T \mathbf{T} \mathbf{D}^{-1} \mathbf{u}}{2u_0^B} + \dots \right] \cdot \underbrace{\delta(u)\delta(v) \left| \frac{\partial(x', y')}{\partial(u, v)} \right|}_{=1, \text{ eq. (66)}} du dv = G(\mathbf{x}), \quad \text{q.e.d.} \quad (67)$$

To summarize the previous derivation, the eqs. (4,5) are satisfied by the white-noise field defined by eq. (56), appropriately scaled with the inflow velocity on the inflow boundary, i.e.,

$$\mathcal{U}^*(\mathbf{x}, t) = \frac{\mathcal{U}(f(\psi(\mathbf{x})), t - \tau(\mathbf{x}))}{\sqrt{u_0^B(f(\psi(\mathbf{x})))}}. \quad (68)$$

Here \mathcal{U} denotes a spatiotemporal white-noise field that is exclusively specified on the inflow boundary and has the covariance given by eq. (49).

To qualitatively understand the meaning of the RHS described through eq. (62), let us consider a shape or 'blob' function with finite support and cross-section dA , which is initially located on the inflow boundary, see the sketch in Fig. 9. If its amplitude is appropriately scaled, it can be deemed to be a finite approximation to a spatial 2D δ -function. If this blob function is freely convected through the mean-flow field, its shape undergoes some distortion. In decelerating flow, for example, it will become squeezed in flow direction but stretched normally to it. Furthermore, the cross-sectional shape could become sheared by the mean-flow. However, in incompressible flow the cross-sectional area dA remains constant. Hence, if the area of the upstream function is 'shrunk' to zero to create a 2D δ -function^b, all distorted downstream blobs similarly become valid 2D δ -functions. This is due to the fact that the δ -function can be constructed from all shape functions, which are positive, localized around a certain point, and whose volume is normalized to one. Hence, for a convective white-noise field that satisfies eq. (5), if the condition eq. (4) is just realized on the inflow boundary, it automatically holds in the remaining interior wetted by the mean-flow. Since this heuristic argument also holds for 3D incompressible flows, it is evident that eqs. (4,5) can also be satisfied in 3D. Furthermore, considering compressible flow, the cross-sectional area of the blob function would change according to the (known) local mean-flow density ρ_0 such that $\rho_0 dA$ rather than dA would remain constant along a streamline (mass conservation in the mean-flow). Hence, in eq. (62) an additional factor ρ_0^B/ρ_0 would appear. Apparently, compressibility could be taken into account by scaling the white-noise field of eq. (68) with an additional factor $\sqrt{\rho_0/\rho_0^B}$.

For convenience, the derivation of the convective white-noise field was based on the definition of an inflow boundary perpendicular to the mean-flow. However, a white-noise field can also be set up for more complex shaped inflow boundaries, which are not oriented normal to the inflow boundary, by adjusting in the discrete realization the local seeding rate appropriately.

^bTo be precise: the limes has to be taken for the integral of the shape function convolved with a test function.

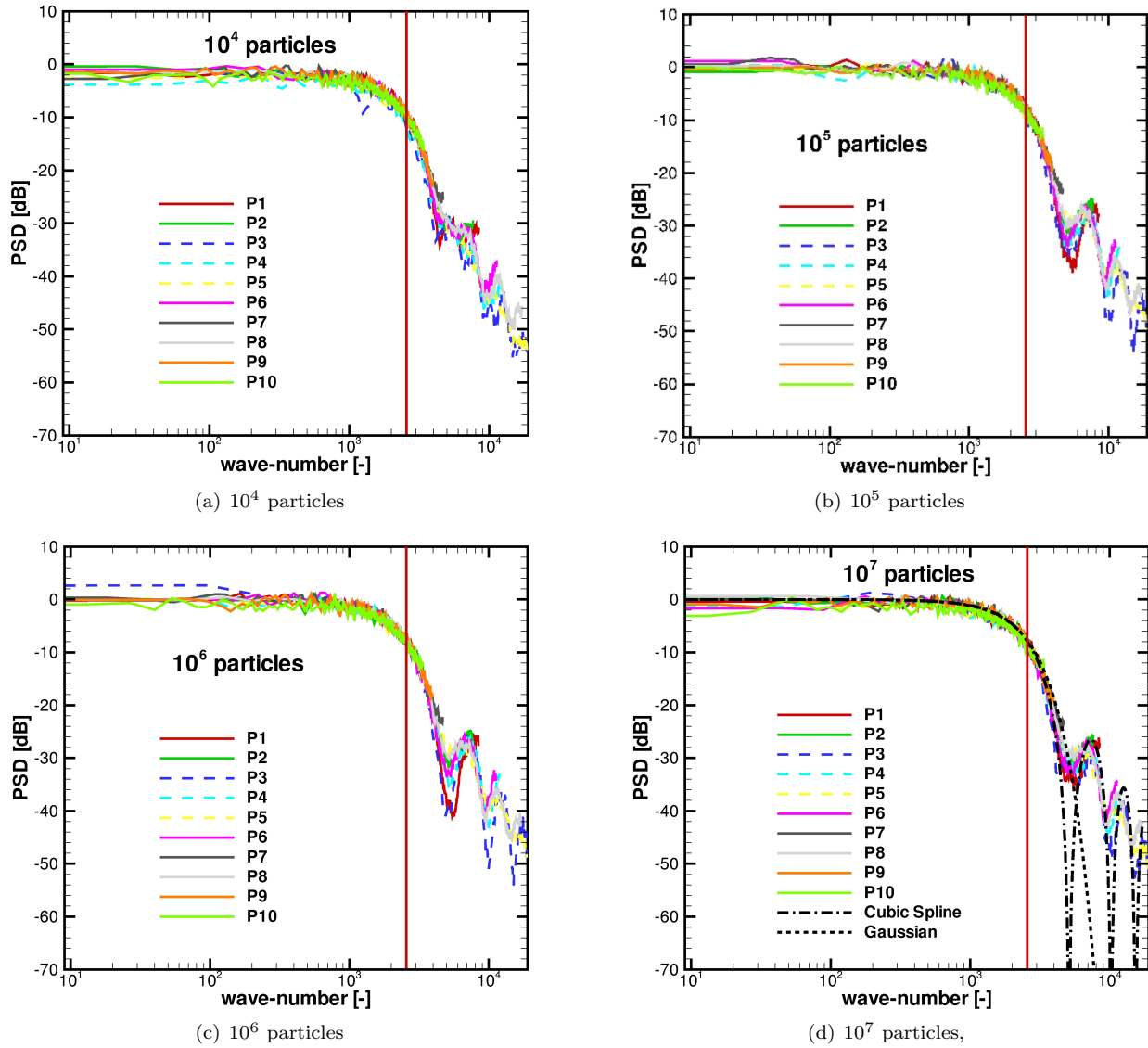


Figure 10. PSD of discrete convective white-noise in 10 observer points on the auxiliary mesh; vertical line: Nyquist mesh cut-off limit; dash-dotted line in (d): spectral density related to the cubic spline correlation eq. (20); dotted line: spectral density related to a Gaussian correlation with correlation length $3/4\Delta$.

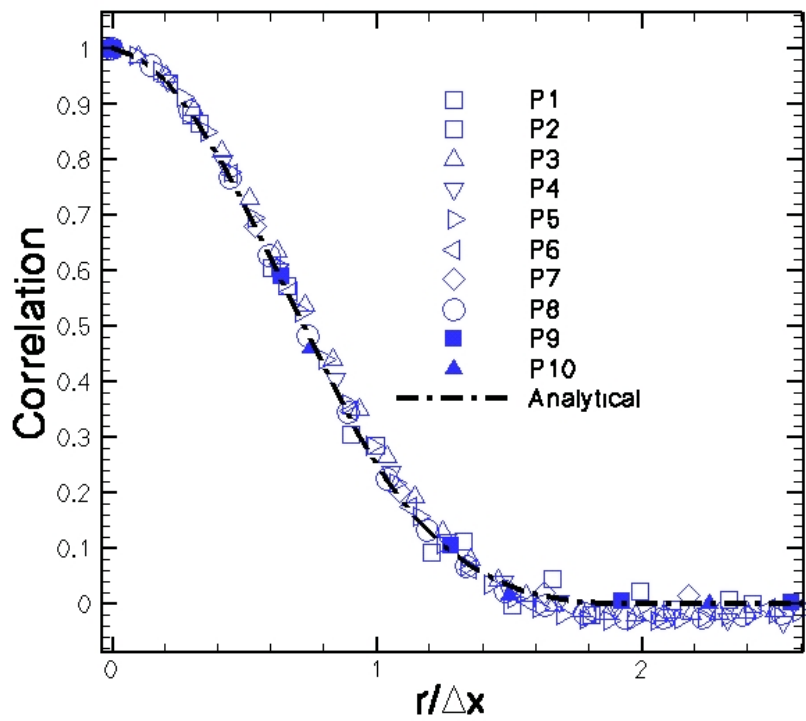
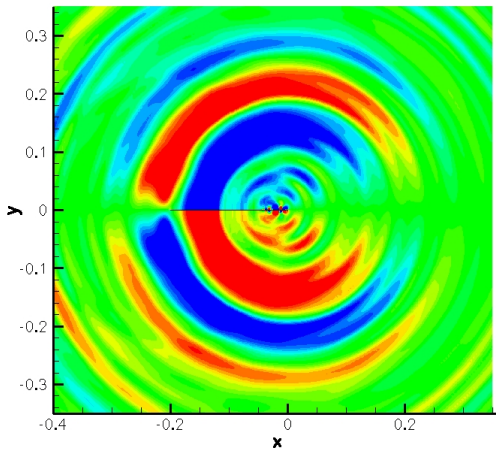
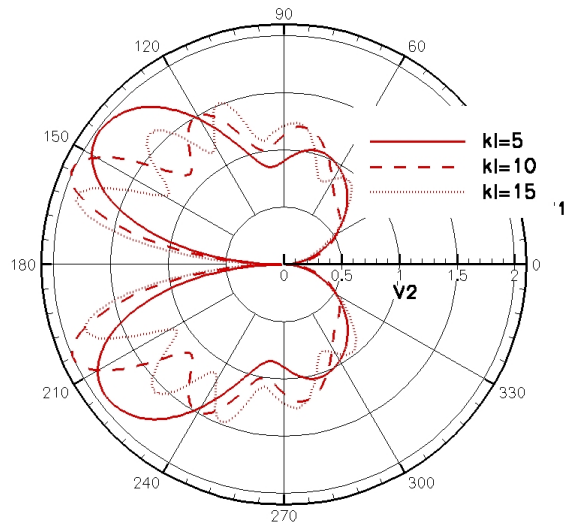


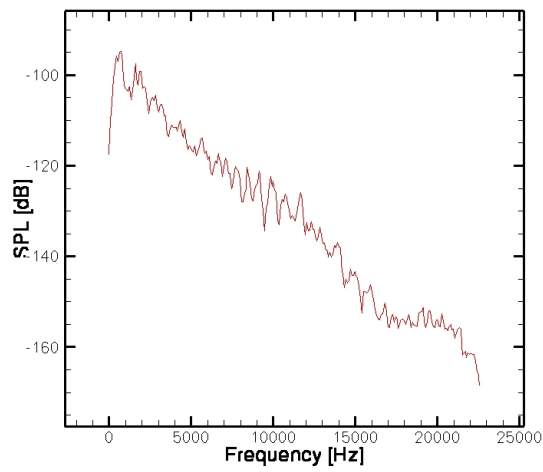
Figure 11. Spatial correlation in 10 observer points on the mesh; dash-dotted line: theoretical cubic spline correlation, eq. (20).



(a) Sound field

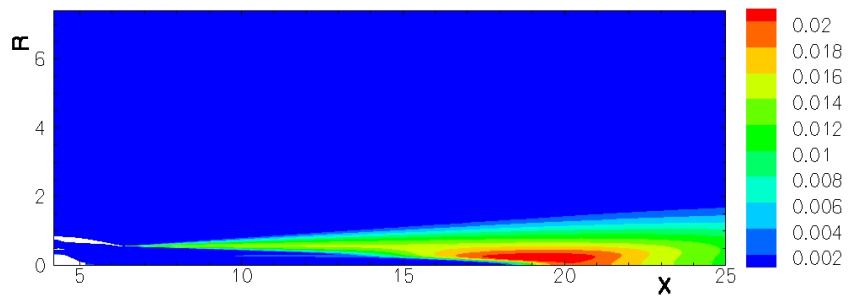


(b) Directivities for different wave-numbers kl

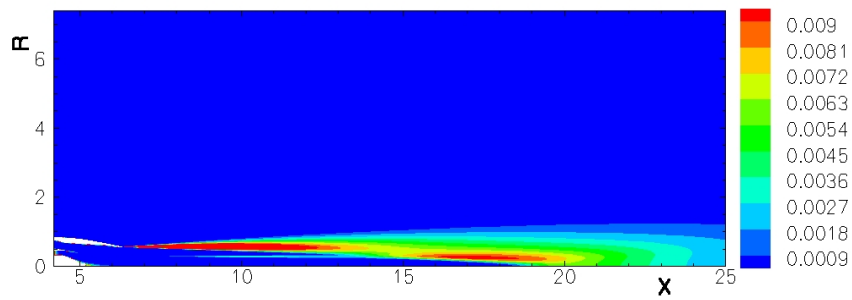


(c) Narrow band spectrum

Figure 12. Flat plate trailing edge noise.

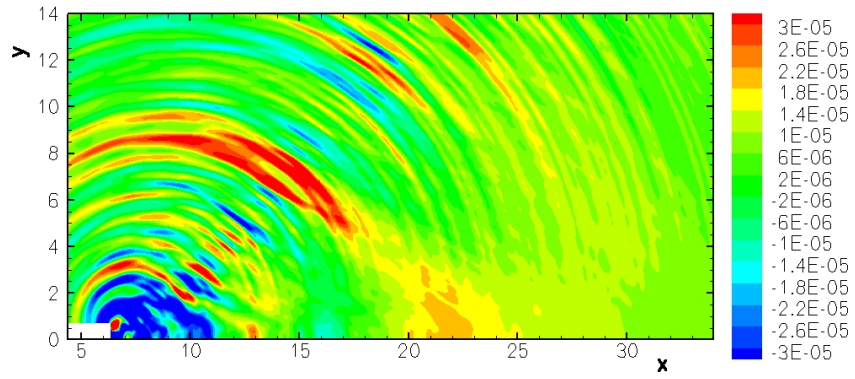


(a) Turbulence kinetic energy

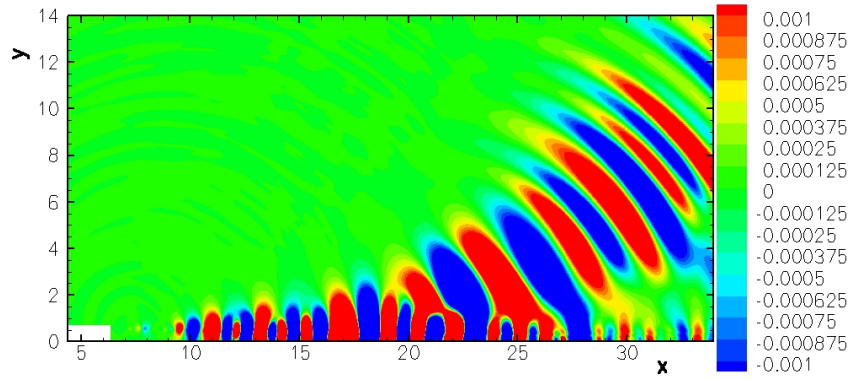


(b) Tam & Auriault source strength $\hat{q}_s/c\tau_s$

Figure 13. RANS results for a jet.



(a) LEE, mean-flow gradients neglected



(b) Full LEE

Figure 14. Jet sound field.

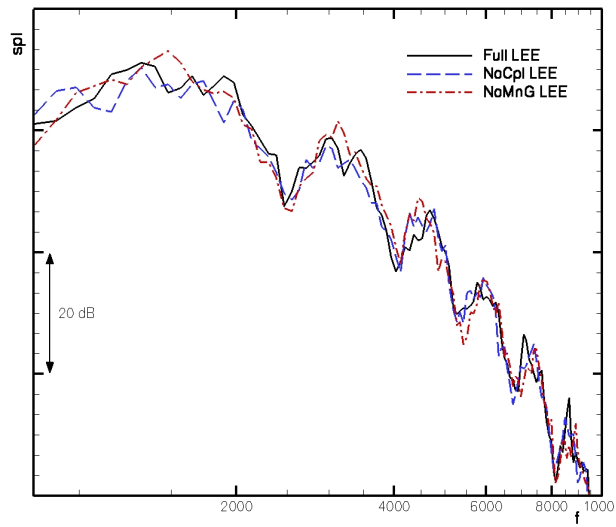


Figure 15. Narrow band spectra at $\theta = 90^\circ$, Full LEE, NoMnG LEE = LEE without mean-flow gradients.

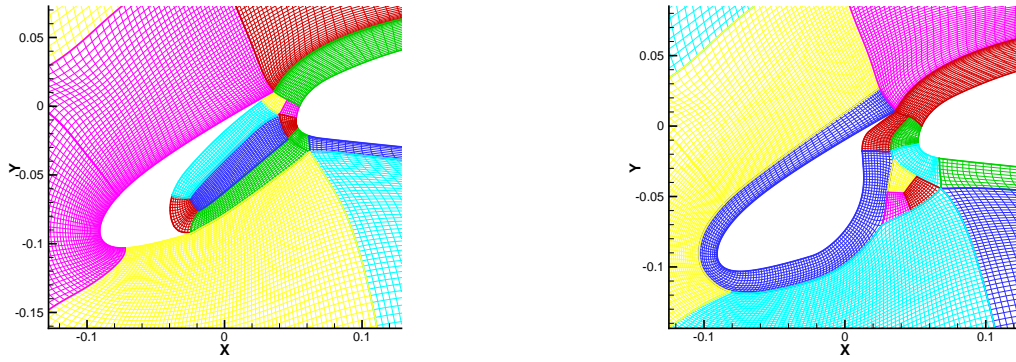


Figure 16. CAA mesh to resolve the slat with and without slat cover cover.

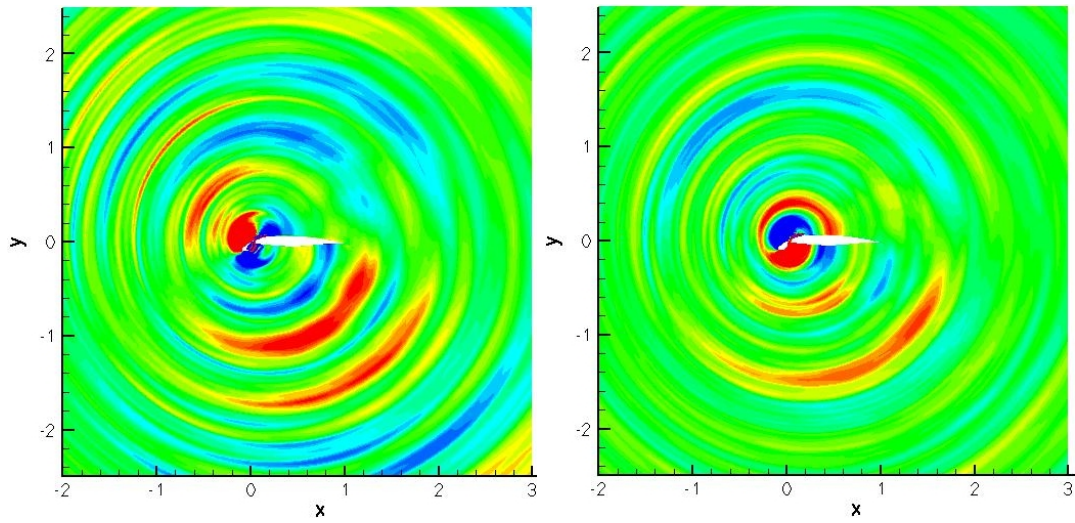
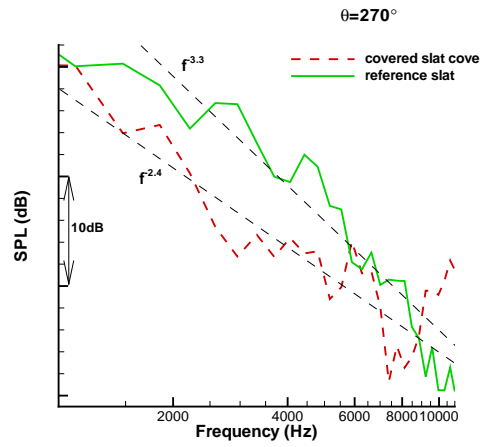
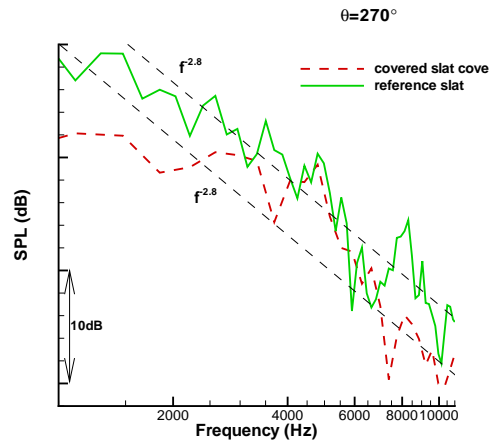


Figure 17. Pressure contours of the reference (left) and the slat cover cover configuration (right).

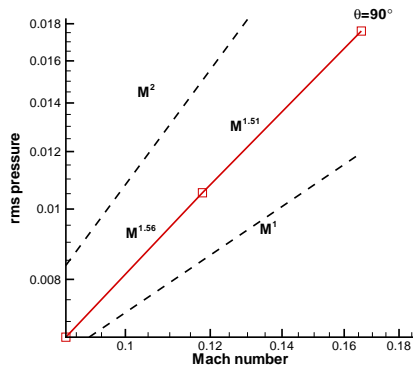


(a) 30m/s flow speed

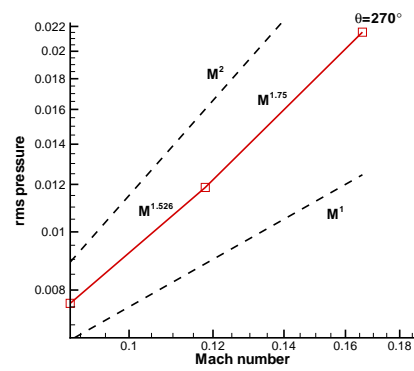


(b) 56m/s flow speed

Figure 18. Sound pressure spectra $r/c = 1.5$ underneath the slat at $\theta = 270^\circ$.



(a) $\theta = 90^\circ$



(b) $\theta = 270^\circ$

Figure 19. Mach number scaling of rms pressure on circle of radius $r/c = 1.5$